



## The high conductivity of iron and thermal evolution of the Earth's core



Hitoshi Gomi<sup>a,\*</sup>, Kenji Ohta<sup>a,1</sup>, Kei Hirose<sup>a,b,c,\*</sup>, Stéphane Labrosse<sup>d,e</sup>, Razvan Caracas<sup>d</sup>, Matthieu J. Verstraete<sup>f</sup>, John W. Hernlund<sup>b,g</sup>

<sup>a</sup> Department of Earth and Planetary Sciences, Tokyo Institute of Technology, Meguro, Tokyo 152-8551, Japan

<sup>b</sup> Earth-Life Science Institute, Tokyo Institute of Technology, Japan

<sup>c</sup> Institute for Research on Earth Evolution, Japan Agency for Marine-Earth Science and Technology, Yokosuka, Kanagawa 237-0061, Japan

<sup>d</sup> Laboratoire de géologie de Lyon, CNRS UMR 5276, Ecole Normale Supérieure de Lyon, Université Claude Bernard Lyon 1, 46 Allée d'Italie, 69364 Lyon Cedex 07, France

<sup>e</sup> Institut Universitaire de France, France

<sup>f</sup> Institut de Physique, Université de Liège, Allée du 6 aout, 17, B-4000 Sart Tilman, Liège, Belgium

<sup>g</sup> Department of Earth and Planetary Science, University of California, Berkeley, CA 94720, USA

### ARTICLE INFO

#### Article history:

Received 22 February 2013

Received in revised form 13 July 2013

Accepted 17 July 2013

Available online 9 August 2013

Edited by M. Jellinek

#### Keywords:

Core

Electrical resistivity

High pressure

Thermal conductivity

Thermal evolution

### ABSTRACT

We measured the electrical resistivity of iron and iron-silicon alloy to 100 GPa. The resistivity of iron was also calculated to core pressures. Combined with the first geophysical model accounting for saturation resistivity of core metal, the present results show that the thermal conductivity of the outermost core is greater than 90 W/m/K. These values are significantly higher than conventional estimates, implying rapid secular core cooling, an inner core younger than 1 Ga, and ubiquitous melting of the lowermost mantle during the early Earth. An enhanced conductivity with depth suppresses convection in the deep core, such that its center may have been stably stratified prior to the onset of inner core crystallization. A present heat flow in excess of 10 TW is likely required to explain the observed dynamo characteristics.

© 2013 Elsevier B.V. All rights reserved.

### 1. Introduction

Earth's magnetic field is re-generated by dynamo action via convection currents in the liquid metal outer core, which are in turn driven by a combination of thermal buoyancy associated with secular cooling (along with possible radioactive heating) and buoyant release of incompatible light alloying components upon inner core solidification. Prior to the crystallization of an inner core, if thermal buoyancy alone drives convection, then the power for maintaining a geodynamo must be in excess of the heat conducted down the isentropic gradient that develops in the presence of convection, placing tight constraints upon the core's thermal evolution (Stevenson, 2003; Labrosse, 2003).

Electrical conduction in metals is impeded by coupling between mobile electrons and the atomic lattice, a process that also dominates heat transfer in metals. This link between electrical resistivity and the electronic contribution to thermal conductivity of metallic iron is expressed through the Wiedemann–Franz law,

$k = 1/\rho \times L \times T$ , where  $k$  is the thermal conductivity,  $\rho$  is the electrical resistivity,  $L$  is the Lorentz number ( $L = 2.44 \times 10^{-8} \text{ W } \Omega/\text{K}^2$ ), and  $T$  is the absolute temperature (Anderson, 1998; Poirier, 2000). While it is a lower bound, this relation provides a good estimate of the total thermal conductivity of metals because other heat transport mechanisms are thought to be small in comparison to electronic heat transport. The effects of pressure, temperature, and impurities on metal resistivity are, however, still poorly constrained by experiments (Stacey and Anderson, 2001; Stacey and Loper, 2007; Bi et al., 2002; Keeler and Mitchell, 1969; Matassov, 1977), although many recent theoretical predictions have been proposed (Sha and Cohen, 2011; de Koker et al., 2012; Pozzo et al., 2012; Pozzo et al., 2013). The resistivity of iron has been examined by static experiments only to  $\sim 40$  GPa (Balchan and Drickamer, 1961; Reichlin, 1983), while the core is subject to pressures of more than 135 GPa.

In this study, we measured the electrical resistivity of pure Fe and Fe–Si alloy (3.90 at.% Si) to 100 GPa in a diamond-anvil cell (DAC). The resistivity of iron was also calculated to core pressures based on density-functional theory. In addition to the impurity resistivity and temperature effects described by the Bloch–Grüneisen formula, we consider the effect of resistivity saturation in the estimates of core resistivity (see Appendix A). While the saturation of metal resistivity is well known in metallurgy, it has never been

\* Corresponding authors at: Department of Earth and Planetary Sciences, Tokyo Institute of Technology, Meguro, Tokyo 152-8551, Japan (K. Hirose). Tel.: +81 357342618 (H. Gomi).

E-mail addresses: [gomi.h.aa@m.titech.ac.jp](mailto:gomi.h.aa@m.titech.ac.jp) (H. Gomi), [kei@elsi.jp](mailto:kei@elsi.jp) (K. Hirose).

<sup>1</sup> Present address: Center for Quantum Science and Technology under Extreme Conditions, Osaka University, Toyonaka, Osaka 560-8531, Japan.

included in the geophysical modeling of core metals. The thermal conductivity of the core, calculated from present estimates of the electrical resistivity with the Wiedemann–Franz law, yields much higher values than conventional estimates (Stacey and Anderson, 2001; Stacey and Loper, 2007) but are generally consistent with those recently predicted by theoretical calculations (de Koker et al., 2012; Pozzo et al., 2012, 2013). We also discuss implications for the possibility of a thermal stratification of the core and its thermal evolution with an approach rather different from these previous studies, based on global energy and entropy balances.

## 2. Methods

### 2.1. High-pressure resistivity measurements

The electrical resistivity was measured at high pressure in a DAC with flat 300  $\mu\text{m}$  or beveled 200  $\mu\text{m}$  culet diamonds. Foils of iron (99.99% purity) and iron–silicon alloy (3.90 at.% Si) with initial thickness of  $\sim 10 \mu\text{m}$  were used as samples. Pressure was determined from the Raman spectrum of the diamond anvil at room temperature (Akahama and Kawamura, 2004). The sample resistance was obtained by the four-terminal method under a constant DC current of 10 mA with a digital multi-meter (ADCMT 6581), which avoids contributions from the electrical leads and contact resistance (Fig. 1). We used gold and iron foils as potential leads in runs #1, 2 and #3, 4, 7, respectively. They were connected with the iron sample by means of spot welding in run #3, 4. For iron–silicon alloy experiments (run #5, 6), the potential leads and sample were prepared as a single foil. A layer of  $\text{Al}_2\text{O}_3$  electrically insulated the sample from the rhenium gasket.

A heating experiment (run #7) was also conducted to 383 K at 65 GPa in a muffle furnace, in order to verify the validity of the Bloch–Grüneisen law at high pressure. Temperature was measured

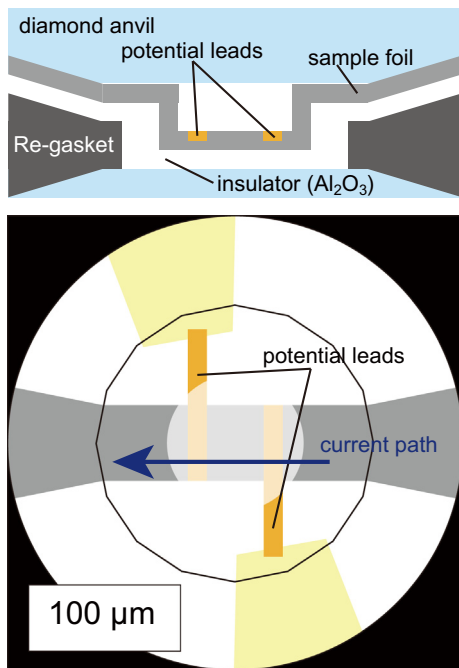


**Fig. 1.** Configuration of the sample and electrodes for electrical resistivity measurements in a diamond-anvil cell. Electronic current passed through the sample foil. Voltage was measured between two potential leads, which gave electrical resistance from Ohm's law. Note that the four-terminal method was used to avoid contributions from electrical leads and contact resistance.

by a thermometer, which was placed very close to the sample. The Bloch–Grüneisen formula describes the effect of temperature on resistivity for a given volume:

$$\rho_{\text{Fe}}(V, T) = B(V) \left( \frac{T}{\Theta_D(V)} \right)^5 \int_0^{\Theta_D(V)/T} \frac{z^5 dz}{(\exp(z) - 1)(1 - \exp(-z))} \quad (1)$$

where  $B(V)$  is a material constant and  $\Theta_D(V)$  is the Debye temperature (Dewaele et al., 2006). It predicts that the change in resistivity is proportional to  $T^5$  at low temperature ( $T < \sim 0.2\Theta_D$ ) and to  $T$  at high temperature ( $T > \sim 0.3\Theta_D$ ), as demonstrated for hcp iron at 22 GPa (Jaccard et al., 2002).

We collected the room-temperature resistance data with decreasing pressure, because the shape and size of the sample and electrodes did not change appreciably during decompression. At the end of each run, the sample resistance was measured at zero pressure. The resistivity ( $\rho$ ) is estimated from the measured resistance ( $R$ ) and sample geometry that is defined by the width ( $w$ ) and length ( $l$ ) between the electrodes and the thickness ( $h$ ) of the iron sample:

$$\rho = R \frac{w}{l} h \quad (2)$$

If the sample geometry changes isotropically by bulk elastic deformation,

$$l = l_0 \left( \frac{V}{V_0} \right)^{\frac{1}{3}}, w = w_0 \left( \frac{V}{V_0} \right)^{\frac{1}{3}}, h = h_0 \left( \frac{V}{V_0} \right)^{\frac{1}{3}} \quad (3)$$

where  $V$  is the volume (subscript zero indicates the value at 1 bar). Eq. (2) is thus rewritten:

$$\rho = \rho_0 \left( \frac{V}{V_0} \right)^{\frac{1}{3}} \frac{R}{R_0} \quad (4)$$

using the known resistivity  $\rho_0$  at ambient conditions,  $1.00 \times 10^{-7}$  and  $3.61 \times 10^{-7} \Omega \text{m}$  for pure Fe and Fe(+3.90 at.% Si), respectively. The volume of iron is taken from the equation of state (Dewaele et al., 2006).

Errors in the present measurements consider two extreme cases of anisotropic deformation. If the geometry changed only along the compression axis (volume change was proportional to the change in thickness):

$$l = l_0, w = w_0, h = h_0 \left( \frac{V}{V_0} \right) \quad (5)$$

therefore,

$$\rho = \rho_0 \left( \frac{V}{V_0} \right) \frac{R}{R_0} \quad (6)$$

which gives a lower bound for the measured resistivity. Similarly, assuming that the geometry changed only in the radial direction (constant thickness):

$$l = l_0 \left( \frac{V}{V_0} \right)^{\frac{1}{2}}, w = w_0 \left( \frac{V}{V_0} \right)^{\frac{1}{2}}, h = h_0 \quad (7)$$

which gives an upper bound upon the sample resistivity:

$$\rho = \rho_0 \frac{R}{R_0}. \quad (8)$$

### 2.2. First-principles calculations

The electrical resistivity of hcp iron was computed from the electron–phonon coupling (EPC) matrix constructed from the electronic wave functions close to the Fermi level, phonon bands, and a

self-consistent deformation potential. All the calculations were based on the density-functional theory (Kohn and Sham, 1965) and the density-functional perturbation theory (Baroni et al., 2001; Gonze et al., 2005) in the ABINIT implementation (Gonze et al., 2002, 2009) with a plane wave basis. In our simulations, we used Troullier–Martins-type pseudo-potentials, a grid of  $20 \times 20 \times 16$  k-points to sample the electron density and a  $4 \times 4 \times 4$  q-point grid for the phonons (Monkhorst and Pack, 1976) and a kinetic energy cutoff of 35 Hartree (1 Hartree = 27.2116 eV). The EPC formalism was developed by Savrasov and Savrasov (1996) and independently implemented in ABINIT. The Boltzmann equations were solved in the lowest order variational approximation. The calculations are non-spin-polarized and were realized using the generalized gradient approximation (Perdew et al., 1996) for the exchange–correlation energy. We perform the calculations at 0 K for several volumes, corresponding to pressures of 40, 80, 120, 200, and 360 GPa.

### 3. Results

We measured the electrical resistivity of iron at high-pressure and room-temperature up to 100 GPa (Fig. 2). A jump in resistivity around 15 GPa is attributed to a phase transition from body-centered-cubic (bcc) to hexagonal-close-packed (hcp) structure (Balchan and Drickamer, 1961). The jump in resistivity at the bcc–hcp phase transition observed in this study is much larger than that predicted by Sha and Cohen (2011) but consistent with the results of earlier static experiments (Balchan and Drickamer, 1961; Reichlin, 1983; Jaccard et al., 2002; Garg et al., 2004). After the phase change, the resistivity diminishes gradually by a factor of four with increasing pressure from 20 to 100 GPa.

Extrapolation of present high-pressure data to ambient pressure gives a resistivity for metastable hcp-Fe of  $5.1 \times 10^{-7} \Omega \text{ m}$ , in good agreement with  $4.4 \times 10^{-7} \Omega \text{ m}$  deduced from earlier measurements at 1 bar by Ohno (1971) (Fig. 2), who reported the resistivity of hcp iron–osmium alloy between 5 and 250 K. The measured resistivity is the sum of a temperature-independent impurity resistivity and a temperature-dependent phonon-contributed resistivity that is described by the Bloch–Grüneisen formula. From Ohno’s data on  $\text{Fe}_{0.8}\text{Os}_{0.2}$ , we calculated the

phonon-contributed resistivity to be  $4.4 \times 10^{-7} \Omega \text{ m}$  at 300 K. This value establishes a lower limit for the resistivity of hcp-iron at 1 bar, because alloying with osmium increases the Debye temperature, which decreases the phonon term in the resistivity. Our DAC experimental results are also consistent with shock compression measurements (Keeler and Mitchell, 1969) (Fig. 2).

Our ambient temperature data is well-fit by the formula:

$$\rho(V, 300 \text{ K}) = F_1 \times \left( F_2 - \frac{V}{V_0} \right)^{F_3} \quad (9)$$

where  $V$  is the volume derived from the equation of state (Dewaele et al., 2006), and  $F_1$ ,  $F_2$ , and  $F_3$  are fitting parameters. In the case of isotropic volume change, we get  $F_{1,\text{Fe}} = 5.26 \times 10^{-9} \Omega \text{ m}$ ,  $F_{2,\text{Fe}} = 1.24$ , and  $F_{3,\text{Fe}} = -3.21$  for hcp-iron. Considering the errors arising from anisotropic deformation of the sample, we obtain  $F_{1,\text{Fe,max}} = 6.51 \times 10^{-9} \Omega \text{ m}$ ,  $F_{2,\text{Fe,max}} = 1.21$ , and  $F_{3,\text{Fe,max}} = -2.85$  as an upper bound, and  $F_{1,\text{Fe,min}} = 3.65 \times 10^{-9} \Omega \text{ m}$ ,  $F_{2,\text{Fe,min}} = 1.30$ , and  $F_{3,\text{Fe,min}} = -4.06$  as a lower bound.

A heating experiment was also performed to 383 K at a pressure of 65 GPa. The measured resistance increased linearly with

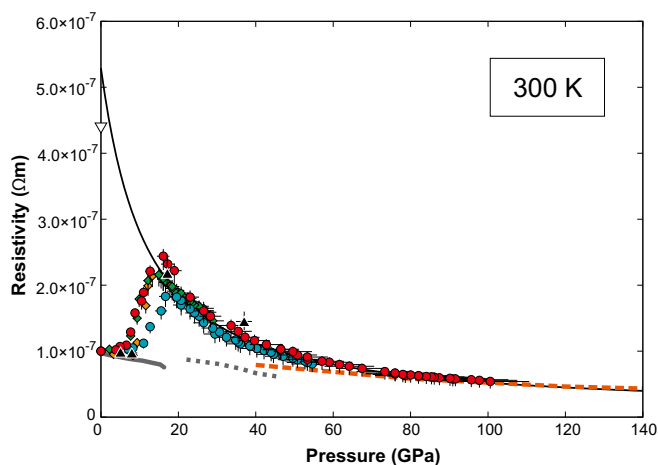


**Fig. 2.** Electrical resistivity of iron as a function of pressure at 300 K. Present DAC results at high pressure, indicated by circles and diamonds, are consistent with the resistivity of hcp-Fe at 1 bar deduced from previous measurement on Fe–Os alloy (open triangle, Ohno, 1971) and shock compression data (closed triangles, Keeler and Mitchell, 1969). Gray solid and broken lines represent earlier first-principles calculations of bcc- and hcp-Fe, respectively (Sha and Cohen, 2011). Our present calculations are shown by the orange dashed line.

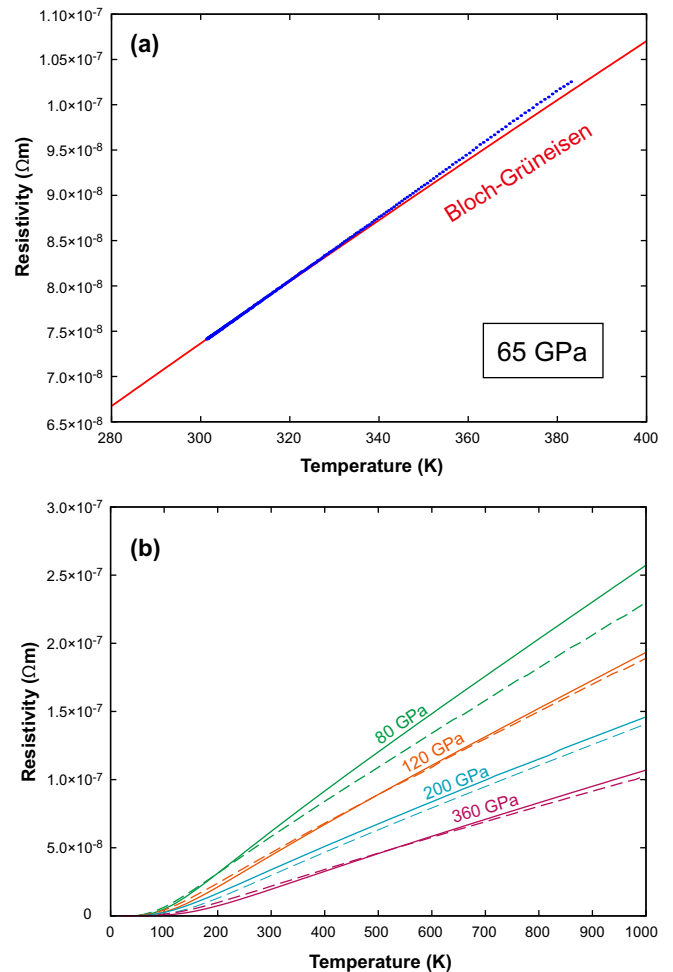


**Fig. 3.** Temperature dependence of the resistivity at high-pressure. (a) Comparison of measured electrical resistivity at 65 GPa (blue dots) with calculations based on the Bloch–Grüneisen law (red solid line). (b) Comparison between the estimates from the present measurements at 300 K and the Bloch–Grüneisen formula (solid lines) and the first-principles calculations (broken lines) below 1000 K, where the saturation resistivity effect is small. All calculations were made under constant volume corresponding to 80 GPa (green), 120 GPa (orange), 200 GPa (blue), and 360 GPa (purple). (For interpretation of the references to color in this figure legend, the reader is referred to the web version of this article.)

increasing temperature (Fig. 3a). These data are in good agreement with the Bloch–Grüneisen law using the reported Debye temperature  $\Theta_D$  (Dewaele et al., 2006).

In addition to experiments, we calculated the resistivity of hcp iron using the electron–phonon coupling from density-functional theory. Our results are in excellent agreement with the present measurements above 50 GPa, and the calculated resistivity at core pressures are consistent with values extrapolated from our experiments using Eq. (9) (Figs. 2 and 3b). Therefore, the decrease in resistivity with pressure reported here is well-supported by both direct experiments and theoretical calculations, and supports the validity of the relationship proposed in Eq. (9).

In order to estimate the effect of alloying components at high pressure, we also measured the resistivity of Fe+3.90%Si (in atomic fraction) to 70 GPa at room temperature (Fig. 4). The results demonstrate that the resistivity of the alloy is significantly greater than that of pure iron at high pressure, and allows us to calibrate a model for the effect of alloying components.

#### 4. Thermal conductivity of the core

The resistivity of iron alloy at core pressure and temperature is estimated in this study from (1) resistivity of iron at high pressure, (2) impurity resistivity of silicon and other light alloying elements, (3) temperature effect following the Bloch–Grüneisen formula, and (4) saturation resistivity. Thermal conductivity is then calculated from the electrical resistivity based on the Wiedemann–Franz law.

##### 4.1. Resistivity of iron

The pressure dependence of the resistivity of iron has been highly controversial. Recent shock-wave studies (Bi et al., 2002) and first-principles calculations (Sha and Cohen, 2011) suggested a simple relation,  $\rho \propto \Theta_D^{-2}$ . This means that the Bloch–Grüneisen formula (Eq. (1)) also predicts the pressure dependence of the resistivity, as the Debye temperature has a volume dependence, with material constant,  $B$ , independent of pressure or volume. On the other hand, Stacey and Anderson (2001) formulated the relation as  $\rho \propto \Theta_D^{-2} \times V^{-2/3}$ , considering an extra factor of electron en-

ergy at the Fermi surface. Later, Stacey and Loper (2007) derived  $\rho \propto \Theta_D^{-2} \times V^{-2/3} \times N^{-1}$ , where  $N$  is the electron density of states at the Fermi level, from the new resistivity data (Bi et al., 2002).

While pressure effects on iron resistivity have been examined in these earlier studies, none of the previously proposed expressions explain the pressure dependence of resistivity observed in this study. We therefore fitted our data to the empirical formula expressed by Eq. (9). The present measurements also indicate that the material constant  $B$  in the Bloch–Grüneisen formula has a volume-dependence.

Our first-principles results are complementary to those of Sha and Cohen (2011), focusing on higher pressures (Fig. 2). In the common range around 40 GPa, we also underestimate the experimental resistivity, but less strongly, and our experimental value is also somewhat smaller than those of Reichlin (1983) and Balog and Secco (1999). The important result here is the convergence of experiment and *ab initio* results at higher pressure. The relatively high resistivity of hcp Fe at low pressure should reflect magnetic fluctuations (Jarlborg, 2002), which is the reason why we find inconsistency between experiments and theory at 40 GPa (note that theory considers non-magnetic hcp Fe). The magnetic and structural fluctuations (e.g., defects, stacking faults) will increase the resistivity. These complications at low pressures do not invalidate our high-pressure calculations on non-magnetic hcp Fe, which agree very well with the room temperature data. At high pressures where the electronic density of states (DOS) is high, the residual magnetic fluctuations are suppressed, and electron-phonon interaction becomes the dominant mechanism governing the resistivity.

##### 4.2. Resistivity and thermal conductivity of iron-silicon alloy

The “ideal” resistivity of the Fe-alloy is given by “Matthiessen’s rule” as the sum of resistivity of pure iron (Eq. (1)) and an additional impurity resistivity:

$$\rho_{\text{ideal}}(V, T) = \rho_{\text{Fe}}(V, T) + \sum_i \rho_i(V) \times \chi_i, \quad (10)$$

where element  $i$  contributes proportionally to its concentration  $\chi_i$  independently of temperature. However, neither the Bloch–Grüneisen formula, nor Matthiessen’s rule, are valid at high resistivity. Instead, the observed resistivity of iron-alloys saturates at a universal value of  $\rho_{\text{sat}} = 1.68 \times 10^{-6} \Omega \text{m}$  at 1 bar with increasing temperature or concentration of impurity (Bohnenkamp et al., 2002) (see Appendix A). With rare exceptions, resistivity saturation occurs in all transition metals when the mean free path  $\lambda$  between electron scattering events becomes comparable to the inter-atomic distance  $x$  (Gunnarsson et al., 2003). The theoretical constraint  $\lambda \geq x$  is known as the Ioffe–Regel condition, and establishes a maximum limit for resistivity in metals called the “saturation resistivity” which is valid over all core temperatures (Milchberg et al., 1988). Saturation is not sensitive to phase transitions, and also occurs in liquid metals. Since the saturation resistivity  $\rho_{\text{sat}}$  depends on inter-atomic spacing, the effect upon iron can be extended to high pressures using:

$$\rho_{\text{sat}}(V) = 1.68 \times (V/V_0)^{1/3} \times 10^{-6} (\Omega \text{m}) \quad (11)$$

In the saturation model, the total resistivity is well-described (Wiesmann et al., 1977) by:

$$\frac{1}{\rho_{\text{tot}}(V, T)} = \frac{1}{\rho_{\text{ideal}}(V, T)} + \frac{1}{\rho_{\text{sat}}(V)} \quad (12)$$

In the limit  $\rho_{\text{ideal}} \rightarrow \infty$ , this model yields the observed behavior  $\rho \rightarrow \rho_{\text{sat}}$ . Multiplying this equation by  $L \times T$  gives:

$$k_{\text{tot}} = k_{\text{ideal}} + k_{\text{sat}} \quad (13)$$

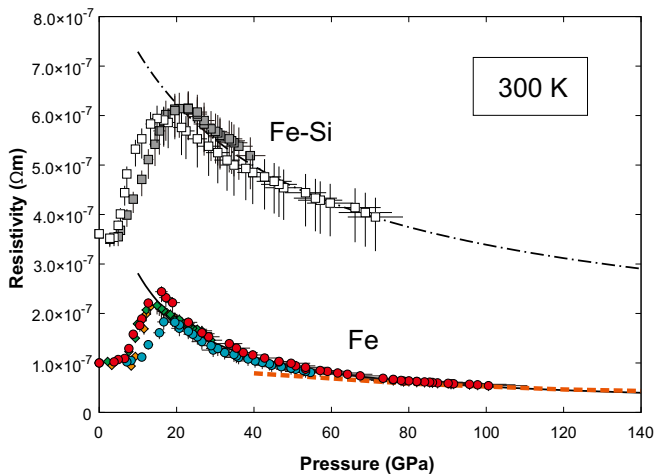


**Fig. 4.** Electrical resistivity of pure Fe and Fe-alloy (4 at.% Si) at high pressure and 300 K. Circles (run #1, 2) and diamonds (run #3, 4) are for Fe, and squares (run #5, 6) are for alloy. Errors in resistivity reflect the uncertainty in sample geometry. Solid and dotted-dashed lines represent the fitting curves (Eqs. (9) and (12) for pure Fe and Fe–Si alloy, respectively). Present first-principles calculations (orange dashed line) reproduce the experimental results at high pressure. (For interpretation of the references to color in this figure legend, the reader is referred to the web version of this article.)

The impurity resistivity of silicon, consistent with the saturation model, can be well-fit by the relation (Fig. 4):

$$\begin{aligned} \rho_{\text{Si}}(V) &= F_1 \times \left(F_2 - \frac{V}{V_0}\right)^{F_3} \\ &= 3.77 \times \left(1.48 - \frac{V}{V_0}\right)^{-3.10} \times 10^{-8} (\Omega \text{m/at.}\%) \end{aligned} \quad (14)$$

Considering potentially anisotropic deformation of the sample, minimum and maximum resistivities of hcp iron–silicon alloy are obtained from Eqs. (6) and (8), respectively. This gives  $F_{1,\text{Si,max}} = 6.29 \times 10^{-8} \Omega \text{m/at.}\%$ ,  $F_{2,\text{Si,max}} = 1.59$ ,  $F_{3,\text{Si,max}} = -3.32$ , and  $F_{1,\text{Si,min}} = 2.21 \times 10^{-8} \Omega \text{m/at.}\%$ ,  $F_{2,\text{Si,min}} = 1.45$ ,  $F_{3,\text{Si,min}} = -3.35$  for Eq. (14).

Earlier static measurements of iron–silicon alloys have been performed only up to 10 GPa (Bridgman, 1957), while shock-wave data are available to 140 GPa (Matassov, 1977). Based on this shock data and Matthiessen's rule, Stacey and Anderson (2001) derived the impurity resistivity of silicon in iron to be  $2.7 \times 10^{-8} \Omega \text{m/at.}\%$ , which is pressure independent. This value is, however, twice as low as  $6.5 \times 10^{-8} \Omega \text{m/at.}\%$  from Bridgman's static data, possibly due to both pressure and saturation effects.

Because our present experiments did not reach saturation, we compared the predictions of our model with previous shock compression data on Fe–Si alloys in which the saturation effect is significant (Matassov, 1977). The results show that the saturation model is in good agreement with the experimental data (Fig. 5).

In general, the resistivity of transition metals exhibits a very minor change upon melting (Cusack and Enderby, 1960; Faber, 1972; Van Zytveld, 1980), which is confirmed by previous large-volume press experiments on iron up to 7 GPa (Secco and Schloessin, 1989). In the case of transition metals, the mean-free path near the melting point is very close to its inter-atomic distance, and therefore the resistivity change is suppressed by the saturation effect (Mott, 1972). Additionally, the validity of the Wiedemann–Franz law has been confirmed for liquid iron at 1 bar (Nishi

et al., 2003). This is consistent with a dominance of heat transport by electrons, as opposed to lattice phonons, in both the liquid and solid state. Thus we consider the resistivity of hcp iron to be a good proxy for the conductivity of liquid iron at core conditions.

Here we estimate the electrical resistivity of the Earth's core from Eqs. (9)–(12), and (14). Assuming silicon as a sole alloying element, the Si content in the outer core is estimated to be 22.5 at.% to account for the 10% core density deficit (Sata et al., 2010). The total resistivity of  $\text{Fe}_{78}\text{Si}_{22}$  is  $\rho_{\text{tot}} = 1.02(+0.04/-0.11) \times 10^{-6}$  for CMB (135 GPa, 3750 K) and  $8.20(+0.54/-1.31) \times 10^{-7} \Omega \text{m}$  for inner core boundary (ICB) (330 GPa, 4971 K) conditions (Table 1). Application of the Wiedemann–Franz law to such resistivity values at high pressure and high temperature gives a thermal conductivity of  $90.1(+9.9/-3.5)$  and  $148(+28/-9) \text{W/m/K}$ , respectively. We find that  $k_{\text{sat}}$  is typically about twice as large as  $k_{\text{ideal}}$ , which emphasizes the importance of saturation, and most importantly also limits the influence of any errors in our treatment of  $k_{\text{ideal}}$ .

#### 4.3. Resistivity and thermal conductivity of other possible iron-alloys in the core

The exact light element composition of the core is presently unknown. We therefore approximate the impurity resistivity of other possible light elements by following the Norbury–Linde rule. While this rule is not confirmed at conditions of Earth's core, it is the simplest way to obtain a first estimate for the conductivity of other alloying components. Norbury (1921) found that the impurity resistivity of some dilute metallic solid solutions is enhanced with increasing horizontal distance between the positions of impurity element and host metal in the periodic table. This implies that (1) impurity elements in the same group exhibit comparable impurity resistivity and (2) group IV elements have larger impurity resistivity than group VI elements for iron-based alloys. On the basis of this relationship, the impurity resistivity of silicon is the same as that of carbon, because both C and Si are group IV

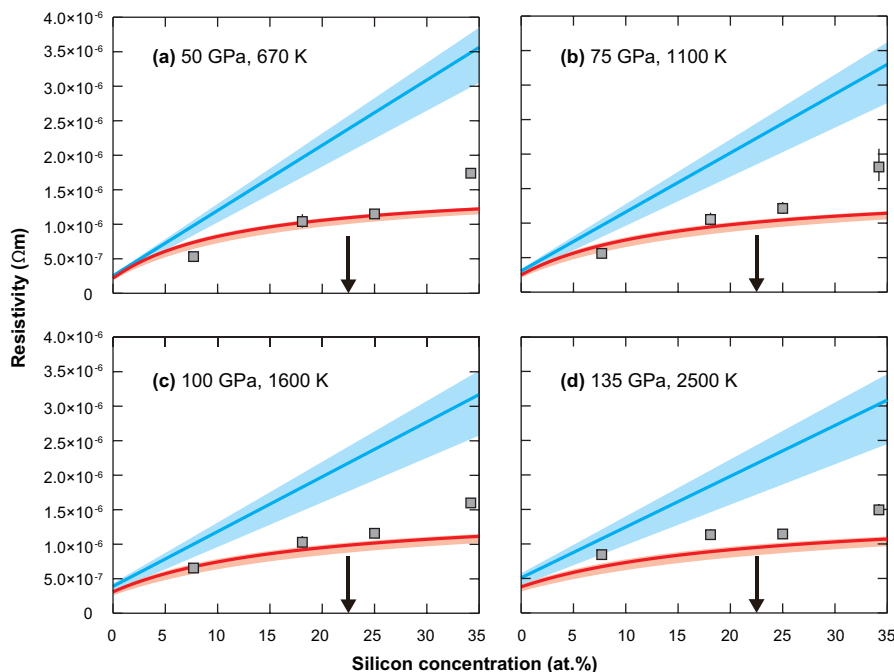


**Fig. 5.** Shock-wave data for resistivity of iron–silicon alloy (square symbol, Matassov, 1977) compared to our estimates with (red, Eq. (12)) and without (blue, Eq. (10)) the saturation effect at (a) 50 GPa and 670 K, (b) 75 GPa and 1100 K, (c) 100 GPa and 1600 K, and (d) 135 GPa and 2500 K. Note that the saturation model better agrees with the previous measurements, particularly for Si concentrations that are relevant for the outer core ( $\chi_{\text{Si}} = 22.5$  shown by arrows). (For interpretation of the references to color in this figure legend, the reader is referred to the web version of this article.)

**Table 1**  
Electrical resistivity of Fe and Fe–Si alloy at high *P–T*.

	101 GPa 2010 K	135 GPa 3750 K (CMB)	208 GPa 5220 K	330 GPa 4971 K (ICB)
Fe				
S & A (theory)		$1.22 \times 10^{-6} \Omega \text{ m}$		$1.12 \times 10^{-6} \Omega \text{ m}$
B (shock exp.)	$6.90 \times 10^{-7} \Omega \text{ m}$		$1.31 \times 10^{-6} \Omega \text{ m}$	
S & C (first-principles)	$5.65 \times 10^{-7} \Omega \text{ m}$		$8.84 \times 10^{-7} \Omega \text{ m}$	$7.5 \times 10^{-7} \Omega \text{ m}$
This study (DAC exp.)	$3.76 \times 10^{-7} \Omega \text{ m}$	$5.37 \times 10^{-7} \Omega \text{ m}$	$5.52 \times 10^{-7} \Omega \text{ m}$	$4.31 \times 10^{-7} \Omega \text{ m}$
Fe <sub>78</sub> Si <sub>22</sub>				
This study		$1.02 \times 10^{-6} \Omega \text{ m}$		$8.20 \times 10^{-7} \Omega \text{ m}$

S & A, Stacey and Anderson (2001); B, Bi et al. (2002); S & C, Sha and Cohen (2011).

elements, and is larger than that of sulfur and oxygen, as both S and O are group VI elements. Indeed, experiments performed at ambient pressure have demonstrated that impurity resistivity of carbon is comparable to that of silicon in bcc iron (Norbury, 1921) and fcc iron (Bohnenkamp et al., 2002). Also, the impurity resistivity of sulfur is insignificant in bcc iron (Bohnenkamp et al., 2002). Oxygen plays a minor role compared to sulfur in liquid copper (Norbury, 1921).

Linde (1932) reported that impurity resistivity for noble metal-based alloys is proportional to  $Z_i^2$ , where  $Z_i$  is the difference in valence between impurity element and host metal. Mott (1936) provided an interpretation for Linde's rule, assuming the impurity atom to be a point charge  $Z_i \times e$ , where  $e$  is the elementary electrical charge. This approximation successfully explains the  $Z_i^2$  dependence of the impurity resistivity, implying that the valence controls the impurity resistivity. Recently, this relationship has been confirmed by *ab initio* calculations for sp impurity in non-magnetic host metal (Mertig, 1999). The magnetic state of hcp Fe is still controversial, however, ferromagnetism is improbable in the present case (Nasu et al., 2002). Therefore, we considered Linde's rule to be valid for hcp iron alloyed with the sp impurity elements of carbon, sulfur, oxygen, and silicon. The impurity resistivity of solute  $i$  is thus written using the impurity resistivity of silicon as:

$$\rho_i(V) = \rho_{\text{Si}}(V) \times \left(\frac{Z_i}{Z_{\text{Si}}}\right)^2 (\Omega \text{ m/at.}\%) \quad (15)$$

In spite of the complicated valence of transition metals, we assume the valence of iron to be eight, and the valence differences are  $Z_{\text{Si}} = Z_{\text{C}} = 4$  and  $Z_{\text{S}} = Z_{\text{O}} = 2$ . On the basis of this relationship, the impurity resistivity of silicon is similar to that of carbon and larger than sulfur and oxygen. Assuming that Norbury–Linde's rule is valid for iron-based alloys, the predicted thermal conductivities are in the range of 84.2–130 and 136–220 W/m/K at the CMB and ICB, respectively (Table 2).

These values are indeed substantially higher than recent conventional estimates: 28 W/m/K for CMB and 29 W/m/K for ICB, proposed by Stacey and Loper (2007). However, if one includes saturation in the estimate of Stacey and Loper (2007), the total conductivity would be similar to our estimate. Resistivity saturation

**Table 2**  
Electrical resistivity ( $\rho$ ) and thermal conductivity ( $\kappa$ ) of iron-alloys.

	135 GPa 3750 K (CMB)		330 GPa 4971 K (ICB)	
	$\rho$ ( $\Omega \text{ m}$ )	$\kappa$ (W/m/K)	$\rho$ ( $\Omega \text{ m}$ )	$\kappa$ (W/m/K)
Fe +22.5 at.% Si	$1.02 \times 10^{-6}$	90.1	$8.20 \times 10^{-7}$	148
Fe +30 at.% C	$1.09 \times 10^{-6}$	84.2	$8.89 \times 10^{-7}$	136
Fe +23.2 at.% O	$7.30 \times 10^{-7}$	125	$5.72 \times 10^{-7}$	212
Fe +19.4 at.% S	$7.04 \times 10^{-7}$	130	$5.52 \times 10^{-7}$	220

The concentration of light element is determined to account for density deficit of the outer core from pure iron by Sata et al. (2010).

also predicts that thermal conductivity must be greater than 60 W/m/K at CMB (Appendix A), which imposes a strong lower limit (Fig. 6). Our values are also in good agreement with recently reported first-principles calculations using the Kubo–Greenwood equation (de Koker et al., 2012; Pozzo et al., 2012, 2013) (Fig. 6 and 7). Such consistency supports the significance of the resistivity saturation effect, which gives a lower bound for the conductivity of Fe alloys. Inclusion of other heat transport mechanisms, albeit small in comparison with the electronic contribution, will only increase the estimate of core thermal conductivity.

## 5. Thermal structure, dynamics, and evolution of the core

We now consider the implications of the large and depth-increasing thermal conductivity results for the structure, dynamics and evolution of the core and deep mantle. The possibility that a large thermal conductivity of the core could make the heat flow down the isentropic temperature gradient overwhelm the amount taken away by mantle convection has been discussed for a long time. Most earlier studies (e.g., Loper, 1978a,b; Gubbins et al., 1979; Stevenson, 1983) proposed that the average temperature profile stays isentropic, implying that the excess heat not removed by the mantle is instead transported downward by compositional convection owing to release of light elements from inner core crystallization. On the other hand, Labrosse et al. (1997) and Lister and Buffett (1998) proposed that the upper part of the core could

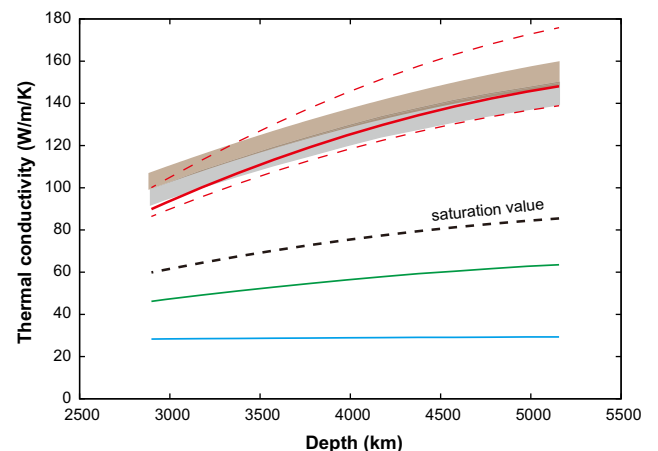


**Fig. 6.** Our estimate of the thermal conductivity of Fe<sub>77.5</sub>Si<sub>22.5</sub> alloy (red solid line) with uncertainties (red broken lines) along an isentropic temperature profile (Stacey and Davis, 2008) compared with previous first-principles (gray, de Koker et al., 2012, Fe<sub>75</sub>Si<sub>25</sub>; brown, Pozzo et al., 2013, Fe<sub>82</sub>Si<sub>10</sub>O<sub>8</sub> for upper limit and Fe<sub>79</sub>Si<sub>8</sub>O<sub>13</sub> for lower limit) and modeling results (green, Stacey and Anderson, 2001, Fe<sub>65</sub>Ni<sub>10</sub>Si<sub>25</sub>; blue, Stacey and Loper, 2007, Fe<sub>65</sub>Ni<sub>10</sub>Si<sub>25</sub>) for similar compositions. The black broken curve indicates the thermal conductivity that corresponds to the saturation resistivity (see text). (For interpretation of the references to color in this figure legend, the reader is referred to the web version of this article.)

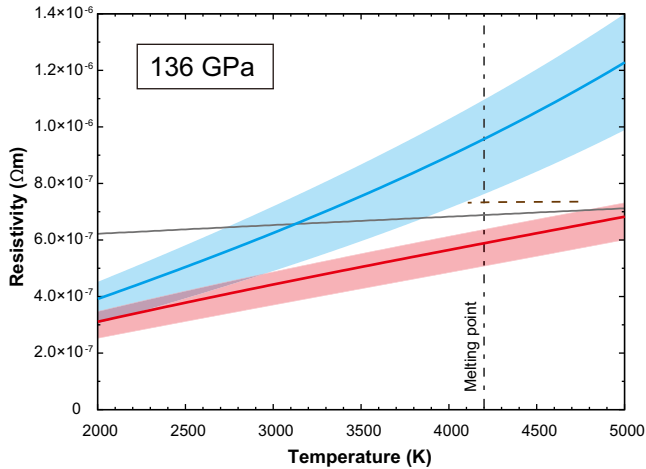


**Fig. 7.** Electrical resistivity of iron at 136 GPa. Red and blue curves are for our model both with and without saturation, respectively. The gray solid line is from [de Koker et al. \(2012\)](#), and the brown broken line is from [Pozzo et al. \(2012\)](#). The vertical broken line is the melting temperature ([Alfè et al., 2002b](#); [Anzellini et al., 2013](#)). Note that our saturation model is consistent with these two recent *ab initio* calculations at core temperatures above the melting point. (For interpretation of the references to color in this figure legend, the reader is referred to the web version of this article.)

develop a stable thermal stratification (i.e., a sub-adiabatic temperature gradient). This possibility has been recently revived by [Pozzo et al. \(2012\)](#) because of the large value of thermal conductivity they obtain. Their analysis is based on the paper of [Davies and Gubbins \(2011\)](#) who computed a buoyancy profile for the core from conduction solutions. This approach is valid when discussing the linear stability of the diffusion solution ([Kono and Roberts, 2001](#)). However, its application to cases with a stably stratified layer overlying a strongly non-linearly driven convective region is questionable. We base our reasoning on different grounds by calculating the energy balance of a suitably defined sub-shell of the core that allows us to compute the profile of finite amplitude convective heat transfer for an isentropic reference state. Our predictions concerning stably stratified layers in the core also differ from that of [Pozzo et al. \(2012\)](#), as discussed below.

We do not consider here any compositional stratification (e.g., [Fearn and Loper, 1981](#)) because, to first order, it should not be influenced by the thermal conductivity. Of course, thermal convection acts against compositional stratification and the two aspects cannot be entirely separated, but treating these questions requires a fully dynamical model and falls beyond the scope of this paper.

**Fig. 8** shows the thermal conductivity profile for a CMB value of 90 W/m/K and the resulting heat flux density, both for the present time and at the onset of inner core crystallization. The increase of the thermal conductivity with depth and the decrease of the isentropic temperature gradient cause the heat flux density to peak at an intermediate depth. Here we show that this situation implies a total convective heat flow that can be negative in a region around the peak value.

Many papers have been devoted to the thermodynamic equations of the geodynamo and their implications for the thermal evolution of the core ([Braginsky, 1964](#); [Gubbins, 1977](#); [Gubbins et al., 1979, 2003, 2004](#); [Buffett et al., 1992, 1996](#); [Braginsky and Roberts, 1995](#); [Lister and Buffett, 1995](#); [Labrosse et al., 1997, 2001](#); [Labrosse, 2003](#); [Nimmo et al., 2004](#); [Nimmo, 2007](#)) and only the salient aspects of the problem will be presented here with a focus on the implications of the high and depth-dependent thermal conductivity obtained in this study. Most of the analysis follows more specifically from the papers of [Lister and Buffett \(1995\)](#), [Braginsky and](#)

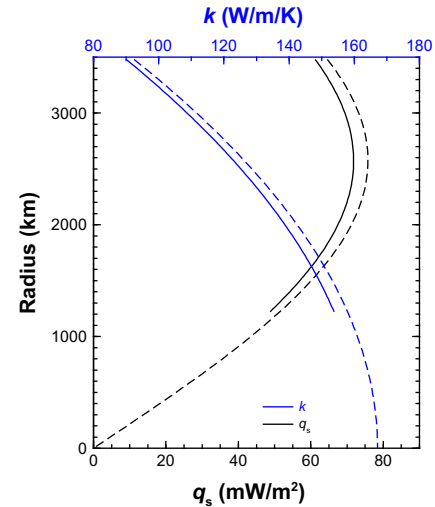


**Fig. 8.** Profiles of the thermal conductivity in the core ( $k$ , blue) and the corresponding isentropic heat flux density ( $q_s$ , black). Note that we consider here the most conservative values of the conductivity obtained in the present study. The solid lines are for the present time whereas the dashed ones are for the time of the onset of inner core crystallization. (For interpretation of the references to color in this figure legend, the reader is referred to the web version of this article.)

[Roberts \(1995\)](#) and [Labrosse \(2003\)](#) which we use to show how profiles for convective heat flow in the core can be computed.

### 5.1. Reference profiles in the core

Following the approach of [Lister and Buffett \(1995\)](#) and [Braginsky and Roberts \(1995\)](#), each quantity  $X$  in the core can be written as the sum of an average radius- and time-dependent profile  $X_a(r, t)$  and the convective fluctuations  $X_c$  around it,

$$X = X_a + X_c. \quad (16)$$

We denote by  $\bar{X}$  the average of  $X$  on the sphere of radius  $r$  and on a timescale long compared to the convective overturn and short compared to the secular evolution. By definition,  $\bar{X}_c = 0$ . As in previous studies, the average state is assumed isentropic and well-mixed, meaning that the specific entropy  $s$  and light element concentration  $\xi$  have a constant average profile. The convective fluctuations in all quantities are very small but when multiplied by the large flow velocity  $v$  they contribute significantly to the global fluxes. In terms of core thermodynamics and compositional buoyancy source(s), the relevant parameter is the difference in mass fraction of light elements across the ICB and  $\xi$  must be understood in that sense. If, as proposed by [Alfè et al. \(2002a\)](#), only oxygen significantly fractionates by crystallizing the core at ICB conditions,  $\xi$  can be considered as the difference in mass fraction of O between the outer core and the inner core.

The specific entropy and mass fraction of light elements being assumed uniform in the mean state, we can write explicit expressions for the temperature  $\bar{T} \equiv T_a(r, t)$  (the isentropic temperature profile, or isentrope), the density  $d$ , the acceleration of gravity  $g$ , the chemical potential  $\mu_a$ , and the coefficients of thermal and compositional expansion  $\alpha$  and  $\beta$ . These follow closely from the work of [Labrosse \(2003\)](#) and are detailed in [Appendix B](#). Each of these profiles depends explicitly on radius and can be expressed in a polynomial form. The time dependence, in particular for the temperature and mass fraction of light elements, is linked to the gradual crystallization of the inner core of radius  $c(t)$ .

The liquidus temperature  $T_L$  is assumed to vary linearly with concentration in light elements and pressure, the latter dependence being assumed to follow Lindemann's law ([Poirier, 2000](#)).

Expressed as a function of radial position (instead of pressure) and inner core radius (instead of concentration), this reads

$$T_L(c(t)) = T_{L0} \left[ 1 - 2 \left( \gamma - \frac{1}{3} \right) \frac{c(t)^2}{H_{comp}^2} \right] + \xi_0 \left( \frac{\partial T_L}{\partial \xi} \right)_p \frac{c(t)^3}{b^3}, \quad (17)$$

$(\partial T_L / \partial \xi)_p$  being assumed constant. The radius of the core is denoted by  $b$ . The gradual change of concentration in light elements in the outer core is computed from the integrated version of Eq. (20) (below), which, to leading order, gives:

$$\xi_a(t) = \xi_0 \left( 1 + \frac{c(t)^3}{b^3} \right), \quad (18)$$

$\xi_0$  being the initial concentration in light elements, before the onset of inner core crystallization.

Having expressed the temperature and pressure profiles in the core, we can compute the thermal conductivity as function of radius. Instead of using the full expressions discussed in the previous sections, we consider an approximate expression which depends linearly on the CMB temperature  $T_{CMB}$  ( $T_{CMBp}$  being its present value), and quadratically on the radial position  $r$ . The present value of the thermal conductivity at CMB conditions,  $k_{CMBp}$ , is used as control parameter. Specifically, we write

$$k = k_{CMBp} \left[ 1 + \frac{k_{6000} - 1}{6000 - T_{CMBp}} (T_{CMB} - T_{CMBp}) \right] \frac{1 - Y_k \left( \frac{r}{b} \right)^2}{1 - Y_k}, \quad (19)$$

the two independent coefficients  $k_{6000}$  and  $Y_k$  being obtained by adjusting the full expression. The value 6000 K has no special meaning here but serves as an arbitrary anchor point for the linear variation of the conductivity with the CMB temperature.

Most parameters used in the calculations are the same as that used by Labrosse (2003), the main exception being the thermal conductivity which is the subject of this paper. These and other parameters' values are listed in Table 3.

## 5.2. Convective heat flow and stably stratified layers

The secular evolution of the average state is controlled by two conservation equations (Eq. (27)a and b of Lister and Buffett (1995)):

$$d_a \frac{d \xi_a}{dt} + \nabla \cdot \overline{d_a \xi_c \mathbf{v}} = -\nabla \cdot \bar{\mathbf{i}}, \quad (20)$$

$$d_a \frac{ds_a}{dt} + \nabla \cdot \overline{d_a s_c \mathbf{v}} = -\frac{1}{T_a} (\nabla \cdot \bar{\mathbf{q}} - \mu \nabla \cdot \bar{\mathbf{i}}) + \frac{\mathbf{J}^2}{\sigma T_a} \quad (21)$$

with  $\mathbf{i}$  the light elements diffusive flux,  $\mathbf{q}$  the heat flux,  $\mathbf{J}$  the electric current density and  $\sigma$  the electrical conductivity. We use total time derivatives for both  $\xi_a$  and the specific entropy  $s_a$  since they are assumed to be uniform with space, except for the jump in  $\xi_a$  across the inner core boundary,  $\xi_a$  being assumed null in the inner core. No radiogenic heating is considered here.

Instead of pursuing this problem in the most general manner (which can be found in the cited literature), we will write down all the simplifying assumptions to avoid carrying along unnecessary complexities. First, we neglect barodiffusion, which is indeed small (Davies and Gubbins, 2011) and Soret diffusion, as well as heat of reaction (dissolution). Compositional diffusion in the average state is also neglected except in boundary layers. These assumptions imply, as constitutive relations for fluxes in the average state:

$$\mathbf{q}_a = -k \nabla T_a; \quad \mathbf{i}_a = 0. \quad (22)$$

These fluxes differ in the boundary layers where they must accommodate the additional convective fluxes. The average thermal state of the inner core is assumed to follow the same isentrope as the outer core for simplicity, which has been shown to provide a good approximation to the diffusion solution as far as the thermal evolution of the outer core is concerned (Buffett et al., 1992; Labrosse et al., 1997, 2001).

With these assumptions, the diffusion terms in Eqs. (20) and (21) read (see Eqs. (30) and (31), using (29) of Lister and Buffett (1995)):

$$\nabla \cdot \bar{\mathbf{i}} = -\xi d_a(c^-) \frac{dc}{dt} \delta(r - c), \quad (23)$$

$$\begin{aligned} \nabla \cdot \bar{\mathbf{q}} = \nabla \cdot \mathbf{q}_a + \left( \frac{Q_{CMB}}{4\pi b^2} - q_a(b) \right) \delta(r - b) \\ - L_{latent} d_a(c^-) \frac{dc}{dt} \delta(r - c), \end{aligned} \quad (24)$$

with  $d_a(c^-)$  the density at the top of the inner core,  $Q_{CMB}$  the total heat flow out of the core, and  $L_{latent} = T_L \Delta S + \mu_{ICB} \xi$  the latent heat of freezing, with  $\Delta S$  the entropy of melting.

We will also use an identity that is well known for convective flows and in particular for the whole core that states that the total dissipation is balanced internally by the work of buoyancy forces:

$$\int_{\Omega} \frac{\mathbf{J}^2}{\sigma} d\Omega + \int_{\Omega_{OC}} (\overline{d_a \xi_a \mathbf{v}} \cdot \nabla \mu_a + \overline{d_a s_c \mathbf{v}} \cdot \nabla T_a) d\Omega = 0 \quad (25)$$

(e.g., Eq. (23) of Lister and Buffett, 1995) with  $\Omega$  the volume of the whole core and  $\Omega_{OC}$  the volume of the outer core. This equation is

**Table 3**  
Parameter values for the thermal structure and evolution calculations.

Parameter	Notation	Value	Notes
Thermal conductivity parameters	$k_{6000}$	1.52182	This study (see text)
	$Y_k$	0.446989	
Core radius	$b$	3480 km	From PREM
Present inner core radius	$c_f$	1221 km	From PREM
Density at the center	$d_0$	12,500 kg m <sup>-3</sup>	From PREM*
Density length scale	$H_{comp}$	7680 km	From PREM*
Grüneisen coefficient	$\gamma$	1.5	From Vočadlo et al. (2003)
Heat capacity	$C_p$	860 J K <sup>-1</sup> kg <sup>-1</sup>	From Stacey (1993)
Entropy of crystallization	$\Delta S$	118 J K <sup>-1</sup> kg <sup>-1</sup>	From Poirier and Shankland (1993)
Coefficient of thermal expansion at the center	$\alpha_0$	1.25 × 10 <sup>-3</sup> K <sup>-1</sup>	This study (see text)†
Bulk modulus at the center	$K_0$	1292 GPa	this study (see text)†
Coefficient of composition expansion	$\beta$	0.67	
Difference in mass fraction of light elements across ICB	$\xi_f$	6%	
Compositional dependence of the liquidus temperature	$\left( \frac{\partial T_L}{\partial \xi} \right)_p$	7333 K	

\* From PREM (Dziewonski and Anderson, 1981) after subtraction of density jump across the ICB and a fit to Eq. (B1).

† From the density expression and thermodynamics relationships.

only valid when the integration is performed on the whole core and expresses a global balance, not a local one.

Integrating the equation for the conservation of light elements (Eq. (20)) over the volume of the core,

$$\int_{\Omega} d_a \frac{d\xi_a}{dt} d\Omega = \frac{d\xi_a}{dt} \int_{\Omega_{oc}} d_a d\Omega = d_a(c^-) \xi_a 4\pi c^2 \frac{dc}{dt}, \quad (26)$$

which simply means that the change of concentration in the outer core is due to inner core growth.

Using this global balance, the total convective flux will be obtained by integrating the equation formed by (Eq. (20))  $\times \mu_a$  + (Eq. (21))  $\times T_a$  over suitably chosen volumes, using the expression for the different fluxes and the global balance just discussed. First, integrated over the whole core volume  $\Omega$ , this gives

$$Q_{\text{CMB}} = - \int_{\Omega} d_a \left( T_a \frac{ds_a}{dt} + \mu' \frac{d\xi_a}{dt} \right) d\Omega + T_L(c) \Delta S d_a(c^-) 4\pi c^2 \frac{dc}{dt} \quad (27)$$

which has the usual form of the global energy balance of the core, used in models of its thermal evolution.  $\mu'$  is the difference between the chemical potential,  $\mu_a$ , and its value at the ICB,  $\mu_{\text{ICB}}$  (see eq. (B4) in appendix). All the source terms on the right-hand side can be expressed as a function of the inner core radius multiplied by its rate of variation (Labrosse, 2003). Compared to the previous papers by Labrosse and coworkers, two modifications have been brought to the model here: the compositional energy term is computed directly from its definition, instead of using the change of gravitational energy (see Braginsky and Roberts (1995), for a discussion on the link between both approaches), and the effect of composition on the liquidus is considered, which modifies the expression of the secular cooling term (e.g., Lister, 2003).

The secular cooling term is computed using the thermodynamic identity  $T \partial_t S = C_p \partial_t T - \alpha T \partial_t P$ , neglecting the second term and by deriving the average temperature profile (e.g., Labrosse et al., 1997).

As shown in previous studies (Labrosse et al., 1997, 2001; Labrosse, 2003), the energy balance equation can be used to compute the growth rate of the inner core for a given CMB heat flow, and this equation is used in the present paper to model the thermal evolution of the core. Now that the equivalence between the local balance equations and the global one has been established (note that the same work can also be done for the entropy equation), we will integrate the energy balance on shells of different sizes to compute the convective flux in the core as a function of radius. Let  $\Omega(r)$  denote the volume of the sphere of radius  $r$  in the core, with  $c \leq r \leq b$ , and  $A(r)$  its surface. Integrating (Eq. (20))  $\times \mu_a$  + (Eq. (21))  $\times T_a$  over  $\Omega(r)$  gives

$$\begin{aligned} & \int_{\Omega(r)} d_a \left( T_a \frac{ds_a}{dt} + \mu_a \frac{d\xi_a}{dt} \right) d\Omega + \int_{A(r)} (\mu_a d_a \bar{\xi}_c \bar{\mathbf{v}} + T_a d_a \bar{s}_c \bar{\mathbf{v}}) \cdot d\mathbf{A} \\ & + \int_{A(r)} \bar{\mathbf{q}} \cdot d\mathbf{A} \\ & = \int_{\Omega(r)} \frac{\mathbf{J}^2}{\sigma} d\Omega + \int_{\Omega(r)} (d_a \bar{\xi}_c \bar{\mathbf{v}} \cdot \nabla \mu_a + d_a \bar{s}_c \bar{\mathbf{v}} \cdot \nabla T_a) d\Omega \end{aligned} \quad (28)$$

Even though, as explained above, the right hand side of this equation only vanishes when the integral is performed on the whole core volume ( $r = b$ ), we will here assume it does so for any value of  $r$ . This assumption can be justified if, on average, the Ohmic and viscous dissipations and buoyancy fluxes are evenly distributed in the outer core. Compressible dynamo calculations could help to test this assumption and any deviation from this even distribution could easily be included in the present theory. Also, the total dissipation is known to be equal to the total convective heat flow (see our Eq. (25), Lister and Buffett, 1995 and Alboussi ere and Ricard, 2013, for a more rigorous demonstration), which is

small compared to the total heat flow at the CMB. The contribution for any radius  $r < b$  can only be an even smaller contribution and neglecting the right-hand-side of Eq. (28) should not be too limiting.

With this assumption, we can express the second integral in Eq. (28), the total convective flux across the surface  $A(r)$ , by computing the other terms. First, as for the computation of the total balance, it is practical to express the balance in light elements by integrating Eq. (20) on  $\Omega(r)$ :

$$\frac{d\xi_a}{dt} \int_{c(t)}^r 4\pi u^2 d_a(u) du + \int_{A(r)} \overline{d_a s_c \mathbf{v}} \cdot d\mathbf{A} = d_a(c^-) \xi_a 4\pi c^2 \frac{dc}{dt}, \quad (29)$$

which can be used to subtract the contribution of  $\mu_{\text{ICB}}$  from Eq. (28). Proceeding as for the global balance, the total convective flow across  $A(r)$  can be expressed for  $c(t) < r < b$ :

$$\begin{aligned} Q_{\text{conv}}(r) & \equiv \int_{A(r)} (\mu' \overline{d_a \xi_c \mathbf{v}} + T_a \overline{d_a s_c \mathbf{v}}) \cdot d\mathbf{A} \\ & = - \int_{\Omega(r)} d_a \left( T_a \frac{ds_a}{dt} + \mu' \frac{d\xi_a}{dt} \right) d\Omega \\ & \quad + T_L(c) \Delta S d_a(c^-) 4\pi c^2 \frac{dc}{dt} - \int_{A(r)} \bar{\mathbf{q}}_a \cdot d\mathbf{A} \end{aligned} \quad (30)$$

This equation shows that the convective heat flow across the surface  $A(r)$  has, by order of appearance on the right hand side, positive contributions from secular cooling ( $Q_{\text{cooling}}$ ), change of compositional energy ( $E_{\text{comp}}$ ) and latent heat ( $Q_{\text{latent}}$ ) but diminished by the heat flow along the isentrope ( $Q_S$ ). Comparison with Eq. (27) shows that if the heat flow across the CMB is exactly equal to the isentropic value, the convective heat flow must tend to zero when  $r$  tends to  $b$ . Each of these terms can be straightforwardly computed from the knowledge of  $dc/dt$ , obtained from  $Q_{\text{CMB}}$  using the global energy balance (Eq. (27)), and the definition of the different profiles. Fig. 9a shows an example of the different contributions to the convective heat flow for a choice of CMB heat flow,  $Q_{\text{CMB}} = 10$  TW, which is slightly larger than the isentropic value. For this specific choice of CMB heat flow, the total convective heat flow is negative over a finite depth range, meaning that this region would tend to become stably stratified. Maintaining a well-mixed isentropic reference state in this region requires convection to transport heat downward. This requires light material (enriched in light elements and/or warm) to have on average a downward velocity, which is rather unlikely. This region should therefore develop a stable stratification, which would make the average profiles deviate from uniform composition and entropy. Penetrative convection from the unstable regions can act against the stable stratification but this effect is estimated to be negligible (see below). Double diffusive convection might also occur (Turner, 1973). A full dynamical treatment is necessary to test this hypothesis and goes beyond the scope of the present study.

Fig. 9b shows that, for a present isentropic heat flow at the CMB  $Q_S(b) = 9.31$  TW, an actual CMB heat flow in excess of 11 TW is necessary to maintain a convective heat flow positive throughout the whole outer core. For lower values of  $Q_{\text{CMB}}$ , a region of the outer core has a negative value of the convective heat flow, either at the top of the core (for  $Q_{\text{CMB}} < Q_S(b)$ ) or at some intermediate depth (for  $Q_S(b) < Q_{\text{CMB}} < 11$  TW). This results entirely from the increase of the thermal conductivity with depth and the associated peak in the isentropic heat flux profile (Fig. 8). A negative convective heat flow means that either (1) this regions stays isentropic, and penetrative convection from adjacent layers manages to transport heat downward, or (2) the region becomes stratified and the average temperature profile is flatter than isentropic, in order to ensure energy conservation with less (or no) convective heat flow. In any case, the region tends to be stably stratified and is here referred to

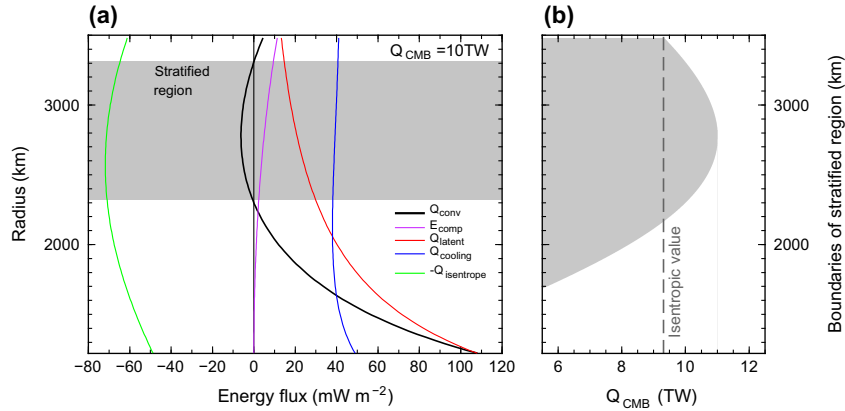


**Fig. 9.** (a) Profiles of the different contributions to the convective heat flux density for a total core heat loss of  $Q_{\text{CMB}} = 10 \text{ TW}$ , slightly larger than the isentropic value: convective heat flux (black), compositional energy flux (purple), latent heat (red), core cooling (blue), and heat conduction along the isentrope (green). The grey area highlights the region where the convective heat flux is negative, leading to thermal stratification. (b) Limits of the stratified region (grey area) as a function of the CMB heat flow, for the present situation with a growing inner core. The dashed vertical line gives the present isentropic heat flow at the CMB. (For interpretation of the references to color in this figure legend, the reader is referred to the web version of this article.)

as the stratified layer. The thickness of the stratified layer depends on heat flow at the CMB as is shown on Fig. 9b for the present state of the core.

### 5.3. Before the inner core crystallization

Before the inner core started to crystallize, the only available buoyancy force is thermal and exists only if the heat flow across the CMB is larger than the isentropic value. The same approach as that presented before can be used, however, since the buoyancy is provided from the top it is more convenient to integrate the equation on the outer shell  $W(r)$  between the sphere of radius  $r$  and the CMB. The equation of energy conservation for this shell can be written as:

$$Q_{\text{CMB}} = - \int_r^b dC_p \frac{\partial T_a}{\partial t} 4\pi u^2 du + Q_{\text{conv}}(r) + Q_s(r) \quad (31)$$

with  $Q_{\text{conv}}(r)$  the heat flow due to convection and  $Q_s(r)$  the heat flow along the average geotherm (both heat flows counted positive upward). At the center, both  $Q_{\text{conv}}$  and  $Q_s$  vanish and, for  $r=0$ , we get the standard global balance for a liquid core. This balance is used to compute the temperature change with time for a given CMB heat flow. The temperature profile entering Eq. (31) is parameterized by the value at the center (Appendix B).

Knowing the rate of core cooling, Eq. (31) can be used to compute the convective power at each radius  $r$  to maintain the isentropic profile as:

$$Q_{\text{conv}}(r) = Q_{\text{CMB}} - Q_{\text{cooling}}(r, b) - Q_s(r). \quad (32)$$

Fig. 10 shows the result of such a calculation for the case where the thermal conductivity at the CMB is  $90 \text{ W/m/K}$  and the heat flow at the CMB is about 30% larger than the isentropic value. The resulting convective power is shown along with the other terms in Eq. (31). One can see that the convective power is positive only in the upper part of such a core. It means that in order to maintain the isentrope down to the center of the core, a downward convective heat flow is required. This is possible energetically, in that the total (mostly Ohmic) dissipation obtained from such a situation is positive, but is likely unrealistic. Instead, the condition of isentropy should be relaxed in the central part. The upper part of the core would be convectively unstable and isentropic but the inner part would be stably stratified and its geotherm would be flatter. Neglecting entirely the possibility of penetrative convection from the upper part to the lower one, the radius of the stably stratified

central core is estimated as the position where the convective heat flow from Eq. (31) is null and is shown on Fig. 10c as function of CMB heat flow.

In this case,  $Q_{\text{CMB}} < Q_s(b)$  implies a negative  $Q_{\text{conv}}$  in the whole core which is entirely stratified since no source of buoyancy exists, which gives the minimum requirement for a dynamo: the heat flow across the CMB must exceed that conducted along the isentrope (a condition known as the Schwarzschild criterion in the astrophysics literature). For  $Q_{\text{CMB}} > Q_s(b)$ , thermal convection can occur in the shallow core but, unless  $Q_{\text{CMB}}$  exceeds about 17.6 TW, the central region of the early core is expected to be thermally stratified.

The CMB heat flow values needed to avoid a thermal stratification are rather large compared to usual estimates (e.g., Lay et al., 2008) and it is therefore likely that the central part of the core could have been stratified for a significant fraction of the pre-inner core history.

### 5.4. Effect of penetrative convection

The problem of penetrative convection from an unstable region to a stably stratified one has received a lot of attention in the astrophysics literature where it arises in the dynamics of stars, for a reason similar to the one discussed here (i.e., the pressure-dependence of the radiative conductivity). Direct numerical simulations have been developed to understand this process (e.g., Hurlburt et al., 1994; Brummell et al., 2002; Rogers et al., 2006), which partly confirmed scaling behaviors obtained earlier by Zahn (1991). We here use the derivation of Zahn (1991) to compute the depth of penetration in the case of interest here.

Considering the energy balance of the penetrative flow and the equilibrium between inertia and buoyancy, Zahn (1991) showed that the penetration height  $H_{\text{penet}}$  scales with the pressure scale height  $H_{\text{press}} = P/dg$  as

$$H_{\text{penet}} = a H_{\text{press}} U_0^{3/2} (6g\alpha T \kappa k_p \nabla_{\text{ad}})^{-1/2}, \quad (33)$$

with  $a < 1$  a coefficient reflecting the geometry of the flow in the unstable region,  $U_0$  the amplitude of the vertical velocity at the boundary between the stable and the unstable layers,  $k_p = (\partial \ln \kappa / \partial \ln P)_S$  and  $\nabla_{\text{ad}} = (\partial \ln T / \partial \ln P)_S$ . Estimating each parameter at the CMB (Table 3), we get  $H_{\text{press}} \approx 1300 \text{ km}$ ,  $k_p \approx 0.25$ ,  $\nabla_{\text{ad}} \approx 0.13$  which gives  $H_{\text{penet}} = a \times 3.9 \text{ km}$ . The parameter  $a$  is unconstrained but (much) lower than unity. The theory on which this estimate is based is simple and, in particular, does not include the effect of

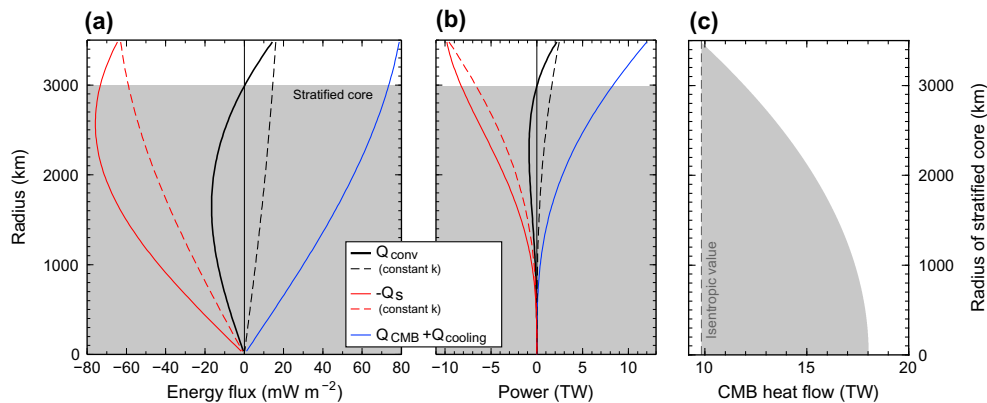


**Fig. 10.** Profiles of the different contributions to the CMB heat flux density (a) and integrated heat flow (b) as a function of position in an assumed fully liquid isentropic core: convective power (black), the sum of core cooling and CMB heat flow (blue) and conduction along the isentrope (red). The dashed lines are the isentropic heat flow and the corresponding convective heat flow if the conductivity is assumed uniform and equal to the CMB value ( $k = 90$  W/m/K). (c) Radius of the stably stratified central region predicted by this calculation as a function of CMB heat flow. (For interpretation of the references to color in this figure legend, the reader is referred to the web version of this article.)

rotation and Lorentz forces, which could increase the coupling between unstable layers and the stably stratified one. When considering a stratified layer in contact with the CMB, lateral variations of the heat flux out of the core would also drive strong thermal wind, although its outcome and the possibility of its observation in the secular variation is still unclear (e.g., Lister and Buffett, 1998; Lister, 2004; Aubert et al., 2007). All of these sources of flow can drive some dynamo action but may not significantly transport heat and solute radially, and therefore may not disturb the larger-scale thermal stratification. The average profiles should lie between the isentropic well-mixed state obtained in strongly driven convection and diffusion profiles that would result from complete stagnation. A better understanding of the resulting thermal structure demands the use of a complete dynamical model, which goes beyond the scope of the present paper.

### 5.5. Thermal evolution calculations

An important implication of the results shown on Fig. 9 is that if the CMB heat flow is lower than the isentropic value, a layer approximately 1400 km thick would tend to develop. This is much thicker than previously envisioned (Gubbins et al., 1982; Labrosse et al., 1997; Lister and Buffett, 1998) and entirely due to the increase of thermal conductivity with depth. Pozzo et al. (2012) also discussed the implications of the large and depth dependent thermal conductivity and their approach and results are compared to ours in Section 5.6.

Several studies have shown that dynamo action is still possible in this case (Stanley et al., 2005; Christensen, 2006; Stanley and Mohammadi, 2008), but affect the resulting magnetic field observed at the surface. For a 1400 km thick stratified layer at the top of the core, we expect the magnetic field generated in the deep core to be greatly filtered by the skin effect in the outer stratified shell, in which case the magnetic field observed at the Earth surface should not follow dynamo scaling (Christensen, 2006). Gubbins (2007) estimated that a maximum thickness of  $\sim 100$  km is acceptable for a stratified layer at the top of the core. We conclude that the present CMB heat flow should exceed the isentropic value. This is also a requirement for thermally driven dynamo action before the existence of the inner core.

Accordingly, in order to study the thermal evolution of the core, we consider the isentropic heat flow at the CMB as the minimum value for the whole magnetic history of the Earth. The thermal evolution is computed with this conservative heat flow history using

the energy balance of the whole core (e.g., Labrosse, 2003). Fig. 11 shows the initial (4.5 Gyr) CMB temperature and heat flow and the age of the inner core as function of the present value of the thermal conductivity at CMB conditions. This shows that the age of the inner core must be less than 1 Gyr, and the initial CMB heat flow and temperature must have exceeded 13 TW and 4500 K, respectively.

Recalling that these are extremely conservative values, allowing for dynamo only in a vanishingly small layer at the top of the core prior to inner core solidification, such a large degree of core cooling implies that a significant portion of the lowermost mantle was extensively molten in the past (Fig. 12), consistent with the presence of a potentially large basal magma ocean in Earth's early history (Labrosse et al., 2007). Our view of melting in the deep mantle has changed significantly in recent years following experimental

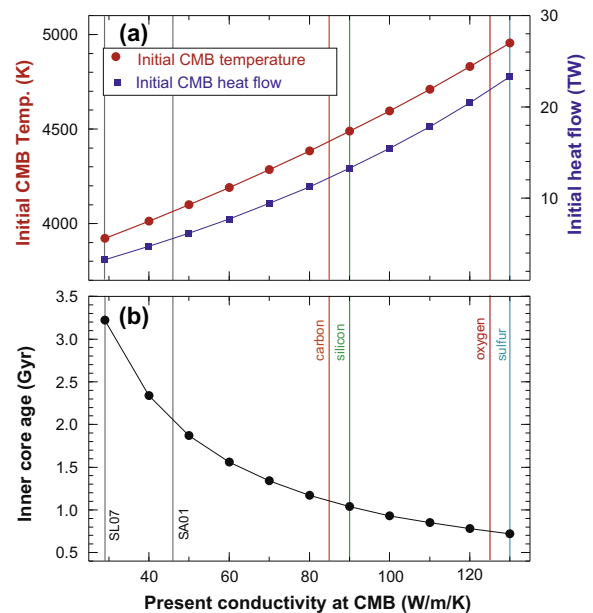


**Fig. 11.** Initial (4.5 Gyr) temperature and heat flow at the CMB (a) and maximum age of the inner core (b) as a function of the present-day thermal conductivity at the top of the core. The calculation assumes the CMB heat flow is equal to the isentropic value at all times, which should be considered a lower bound. Our estimate of the CMB conductivity is indicated for each impurity element. SL07 (Stacey and Loper, 2007) and SA01 (Stacey and Anderson, 2001) show the earlier estimates.

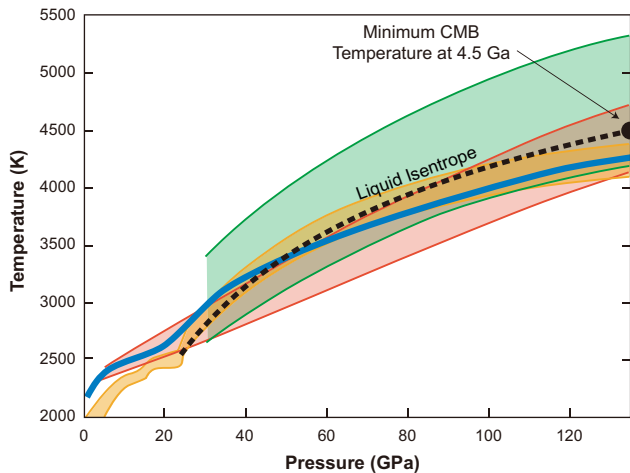


**Fig. 12.** Liquid isentrope with minimum CMB temperature at 4.5 Ga (de Koker and Stixrude, 2009) compared with melting intervals of chondrite (red, Andraut et al., 2011), peridotite (green, Fiquet et al., 2010; yellow, Stixrude et al., 2009), and  $\text{Mg}_2\text{SiO}_4$  (blue, Mosenfelder et al., 2007). The initial CMB temperature exceeds the melting temperature of the mantle, indicating extensive lower mantle melting in the early Earth. (For interpretation of the references to color in this figure legend, the reader is referred to the web version of this article.)

(Nomura et al., 2011) and theoretical (Stixrude et al., 2009) evidence that such melts could be denser than silicate solids and therefore stably persist over geological time scales. Many previous studies have attempted to avoid melting of the early lower mantle by including radioactive sources, such as potassium, in the core (Nimmo et al., 2004). Inclusion of internal heating in the core would reduce its implied initial temperature. However, with a maximum potassium concentration of about 100 ppm (Murthy et al., 2003), producing 0.66 TW presently and 8 TW 4.5 Gyr ago, the initial temperature can be decreased by only  $\sim 200$  K for a minimal CMB heat flow. With the high thermal conductivity values reported here, large degrees of core cooling are therefore unavoidable, and must be incorporated into models of the evolution and structure of the deep Earth.

### 5.6. Comparison with previous studies

Thermal stratification in the core due to a large thermal conductivity has been discussed for a long time (Gubbins et al., 1982; Labrosse et al., 1997; Lister and Buffett, 1998). Assuming the thermal conductivity to be uniform in the core, these early studies considered only a stratification developing at the top of the core, where the isentropic temperature gradient is largest. Also, its value was generally considered to be less than 60 W/m/K. Recently, de Koker et al. (2012) and Pozzo et al. (2012) obtained much larger values, with a large increase with depth in the core, similarly to the results presented above. They discussed the implications for the core thermal structure and evolution and, in particular, proposed that parts of the core could be thermally stratified, as done in the present study. However several important differences on the approaches used and the implied findings need to be discussed.

de Koker et al. (2012) represented (their Fig. 3 bottom) profiles of the total heat flow conducted down the core isentrope for different possible compositions and compared this value to estimates of the CMB heat flow. They find that the CMB heat flow is likely lower than the isentropic value and conclude that the top of the core is stably stratified. Excluding any buoyancy source at depth, they nevertheless state that convection would occur in the deep core. The situation they discuss is similar to the one treated above before crystallization of the inner core (Section 5.3) and we show clearly

that, in this situation, convection can only occur at the top of the core, provided of course that the CMB heat flow is larger than the isentropic value. We also show that a thermal stratification is likely to occur in the inner region. Moreover, despite similar values of thermal conductivity, the values they propose for the isentropic heat flow is significantly different than ours in several ways. Their CMB values are about 50% larger than ours (13 TW for  $k = 90$  W/m/K compared to our value of 9.3 TW), likely because they use different values for the thermal expansion coefficient or the heat capacity. Also, the shape of their isentropic heat flow profiles can be compared to our red curves in our Fig. 10b. Their profiles do not change concavity with depth in the core, similarly to our dashed profile obtained for a uniform conductivity. The depth increase of conductivity is at the origin of the inflection point seen on the solid red profile of Fig. 10 and creates the possibility of a thermally stratified layer at intermediate depth in the core.

Pozzo et al. (2012) propose a much more complete study of the possible thermal stratification of the core. They use a completely different approach based on buoyancy profiles determined as solutions to diffusion equations matching the global balance for the core. This approach, following the papers of Davies and Gubbins (2011) and Kono and Roberts (2001) is fully understandable when considering the linear stability of the diffusion problem but raises some questions when dealing with a stratified region bounded by regions convecting in the non-linear regime. Instead, we consider rigorous energy and entropy balances with strictly identified assumptions, an isentropic reference state and uniformly distributed or small dissipation.

The results from their study and ours also differ significantly, although both discuss the likelihood of thermal stratification. Pozzo et al. (2012) obtain a thermal stratification only at the top of the core, as do earlier studies of the subject. In particular, when considering a CMB heat flow exactly equal to the isentropic value (their case 5), they obtain thermal convection in the whole core. For the same situation, we get a thick thermally stratified layer at the top of the core (Fig. 9) because of the increase with depth of the thermal conductivity. In the case of a CMB heat flow only slightly super isentropic, we show that a thermal stratification can develop at intermediate depth, a possibility not considered by Pozzo et al. (2012). These differences derive from different theories for the stratification of the core and should be tested in the future by use of fully dynamical calculations.

Another important difference between our work and that of Pozzo et al. (2012) concerns the value used for the thermal conductivity. Pozzo et al. (2012) only consider pure Fe and find values consistent with ours. In Pozzo et al. (2012)'s paper, the composition of the core only affects the conductivity through its effect on the core isentrope. When modeling the core thermal structure and evolution we take into account the effect of light elements, which decreases significantly the thermal conductivity. Accordingly, our value for the isentropic CMB heat flow is smaller than that of Pozzo et al. (2012), which makes the thermal evolution calculations less extreme in their outcome. Pozzo et al. (2012) prefer to avoid a large core cooling and young inner core and resort for that on a huge amount of radiogenic heating, between 6 and 13 TW. We consider these values unrealistic (McDonough, 2003) and prefer to consider the implications of a large core cooling, in particular an early thick basal magma ocean (Labrosse et al., 2007).

## 6. Conclusions

We measured the electrical resistivity of iron at room temperature up to 100 GPa in a DAC. While a sharp resistivity increase was observed during the bcc to hcp phase transition, the resistivity diminished with increasing pressure above 20 GPa in the stability

range of the hcp phase (Fig. 2). A heating experiment was also conducted, which confirmed the Bloch–Grüneisen law up to 383 K at 65 GPa (Fig. 3a). We also performed first-principles calculations up to 360 GPa and 1000 K. These experimental and first-principles results show an excellent agreement with each other at high pressure (Figs. 2 and 3b). The resistivity was measured for Fe +4 at.% Si to 70 GPa at 300 K, demonstrating a large effect of Si impurity (Fig. 4).

We modeled the resistivity of iron alloys in the core, considering the effects of (1) pressure and temperature, (2) impurity resistivity of silicon and other possible core light alloying elements, and (3) resistivity saturation. Our model successfully reproduces previously reported shock wave data (Matassov, 1977) (Fig. 5). This is the first study that considers the saturation resistivity in geophysical literature, although it is a well-known effect in metallurgy (see Gunnarsson et al., 2003 for a recent review). The most important consequence of the saturation is that the resistivity of almost all kinds of metals cannot exceed  $\sim 1.5 \mu\Omega \text{ m}$ . This imposes a lower limit on the core's thermal conductivity through the Wiedemann–Franz law. Assuming that silicon is the single light element in the core, the core conductivity is estimated to be  $90.1(+9.9/-3.6)$  and  $148(+28/-9) \text{ W/m/K}$  at CMB and ICB, respectively. In order to evaluate the impurity resistivity of sulfur, oxygen, and carbon, we apply Norbury–Linde's rule for iron-based alloys as a rough estimate. Predicted thermal conductivities are in the range of 84.2–130 and 136–220 W/m/K at the CMB and ICB, respectively (Table 2). These values are substantially higher than the conventional estimates of 28 and 29 W/m/K (Stacey and Loper, 2007), but consistent with recent first-principles calculations (de Koker et al., 2012; Pozzo et al., 2013) (Fig. 6).

We further consider the structure, dynamics, and evolution of the core from our findings of a large and depth-increasing core conductivity. The radial profile of conductive heat flux density has a maximum at intermediate depth in the core, which implies that a CMB heat flow equal to the isentropic value is not sufficient to drive whole core convection in the absence of other buoyancy sources (Fig. 8), contrary to the situation where the thermal conductivity is uniform with depth. Therefore, we calculate the convective heat flow across the spherical shell of each radius from energy conservation. In the present situation with a growing inner core, more than 11 TW of CMB heat flow is required to maintain a positive convective heat flow throughout the entire core. A negative convective heat flow means either this layer is stably stratified with a flatter temperature gradient than isentropic or is penetrated from adjacent layers. However, our estimate of the depth of penetrative convection length is shorter than a few kilometers. We also find that, in the case of a CMB heat flow larger than the isentropic value ( $\sim 9 \text{ TW}$ ) and smaller than 11 TW, a stratified layer is formed at intermediate depth (Fig. 9). Before the birth of the inner core, no convection occurred if the CMB heat flow was less than the isentropic value. If the CMB heat flow was larger than the isentropic value but smaller than 18 TW, thermal convection occurred at the top of the core, in a layer whose thickness increases with the value of the CMB heat flow (Fig. 10). Considering that the CMB heat flow was always higher than the isentropic value throughout Earth's history, we compute the thermal evolution of the core, showing that the age of the inner core must be less than 1 Gyr and that the initial CMB heat flow and temperature must exceed 13 TW and 4500 K, respectively. It suggests that the lowermost mantle must have been molten during the early Earth, which is consistent with the basal magma ocean model (Labrosse et al., 2007) and numerous recent experimental determinations of Earth's mantle solidus (Fig. 12).

## Acknowledgments

We thank T. Komabayashi for discussions and Francis Nimmo and an anonymous reviewer for valuable comments. S.L. and R.C.

are grateful to the LABEX Lyon Institute of Origins (ANR-10-LABX-0066) of the Université de Lyon for its financial support within the program “Investissements d'Avenir” (ANR-11-IDEX-0007) of the French government operated par the National Research Agency (ANR). S.L. has been supported by the Agence Nationale de la Recherche under the grant ANR-08-JCJC-0084-01. J.H. was supported by the National Science Foundation (NSFEAR0855737).

## Appendix A. Significance of saturation resistivity

Saturation resistivity imposes strong limitations on core resistivity. This study is the first to incorporate the saturation resistivity effect into a model for the electrical and thermal conductivity of the Earth's core. For pressures, temperatures, and impurity concentrations relevant to Earth's core, our model is significantly more sensitive to saturation resistivity than it is to measurements of resistivity at ambient temperature and high pressure. In particular, increasing the ambient temperature resistivity measured in the experiments by  $2\times$  reduces the predicted CMB conductivity value by only 5%, while a  $2\times$  increase in saturation resistivity reduces the predicted CMB conductivity by 33%. However, if the Ioffe–Regel condition remains valid at core conditions, then significant errors in  $\rho_{\text{sat}}$  should arise only if its value is different in hcp iron than in both the bcc and face-centered-cubic (fcc) iron phases for which it was measured. Because of the importance of this contribution to the present study, we give a brief overview of the saturation resistivity effect, and how it implies fundamental limitations for the electrical resistivity (and thermal conductivity) of Earth's core.

Metals are commonly known to exhibit a small electrical resistivity in comparison to insulating materials. The transition between metallic and insulating resistivity is discontinuous, and research on relatively high electrical resistance metals and their alloys has revealed that they exhibit a maximum resistivity of  $\sim 1.5 \mu\Omega \text{ m}$ , with only rare (although industrially important) exceptions.

There exists an extensive literature on the subject of saturation resistivity (see Gunnarsson et al., 2003 for a recent review), with support from resistivity measurements on a variety of metals as well as from the theory of electrical conduction. The saturation effect is observed both in cases where the temperature is increased sufficiently to induce high resistivity, as well as in cases where higher resistance is induced by the addition of high resistivity alloying components. The saturation resistivity is similar in magnitude for most transition metals and alloys (Bohnenkamp et al., 2002), and it is insensitive to phase transitions and melting (Mott, 1972) as well as order-disorder transitions (Mooij, 1973). The *ab initio* theory describing resistivity saturation is involved (Gunnarsson et al., 2003), and goes beyond the Boltzmann transport we use here – we therefore do not attempt to compare our *ab initio* resistivities with the data for  $T > 1000 \text{ K}$  which exhibits saturation.

Theoretical justification for the saturation effect dates back to the work of Ioffe and Regel (1960), who noted that the semi-classical theory for electrical resistivity in broadband metals, which invokes electron scattering at sites in the atomic lattice, does not work in the limit of high resistance because the implied mean length scale between electron scattering events  $\lambda$  must eventually become smaller than the inter-atomic distance  $x$ . In the absence of other scattering mechanisms, this model implies that metals exhibit a maximum resistivity, and they proposed that  $\lambda \geq x$ , which we call the “Ioffe–Regel condition”. Gurvitch (1981) used this condition to theoretically derive the parallel resistor formula in Eq. (12), in agreement with Wiesmann's (1977) empirical description of the saturation effect. This condition is derived by assuming that electron–electron interactions are not important

(Gunnarsson et al., 2003). Non-ideal electron behavior is thought to give rise to phenomena such as super-conductivity in metals, however, we do not believe this is important in the Earth's core.

This study is also the first time, to our knowledge, that the saturation resistivity has been extrapolated to high pressure. Our extrapolation relies upon theoretical expressions for the saturation resistivity, such as the one given in Gurvitch (1981):

$$\rho_{\text{sat}} = \frac{1.29 \times 10^{18}}{n^{2/3} x} (\mu\Omega\text{cm}) \quad (\text{A1})$$

where  $n$  is the free electron density measured in units of  $\text{cm}^{-3}$  and the inter-atomic distance  $x$  is measured in Angstroms. For a constant number of conduction electrons per atom, this expression suggests that saturation resistivity scales only with volume as  $\rho_{\text{sat}} \propto V^{1/3}$ , which is what we use in our present model.

We consider whether the assumption of a constant number of conduction electrons per atom is justified for extrapolation to conditions of Earth's core. The usual effect of pressure is to increase the population of electrons in the conduction band, or promote metallic behavior in elements that are insulators at lower pressures. For example, pure oxygen undergoes an insulator-metal transition at pressures of  $\sim 1.2$  Mbar and 4500 K (Bastea et al., 2001). If the number of electrons per atom can only increase with pressure, then the saturation resistivity we use at high pressure is only strictly an upper bound. However, this also means that thermal conductivity estimates derived from strongly saturated resistivity will be a lower bound, and can only be upwardly revised.

The present saturation resistivity model for iron alloys extended to high pressure implies a saturation lower bound for the thermal conductivity of the Earth's core that is entirely independent of measurements of electrical resistivity at low temperatures and low alloy concentrations. This lower bound is obtained in the limit of vanishing ideal conductivity,  $k_{\text{ideal}} \rightarrow 0$ , for which Eq. (13) gives  $k \rightarrow k_{\text{sat}}$ . The values of  $k_{\text{sat}}$  at volumes relevant for the CMB and ICB are 60 and 85 W/m/K, respectively. These values should be considered extreme lower bounds for thermal conductivity, and are valid independent of any measurements of resistivity at lower temperatures and alloy concentrations.

Stacey and Loper (2007) estimated a value for  $k_{\text{ideal}}$  of 29 W/m/K (which is uniform with depth in their model). If they had included the saturation resistivity, they would have obtained total conductivity values of 89 and 114 W/m/K at the CMB and ICB, respectively. Indeed, these values are not very different from the 90.1(+9.9/−3.6) and 148(+28/−9) W/m/K at the CMB and ICB obtained in the present study. Therefore, much of the difference between the estimates in previous studies and the present study is due to inclusion of the saturation effect.

## Appendix B. Average profiles in the core

The average profiles in density  $d$ , gravity  $g$ , temperature  $T_a$ , and chemical potential  $\mu_a$  are obtained from simple integration and can be written in polynomial form as (e.g., Labrosse et al., 2001; Labrosse, 2003):

$$d_a = d_0 \left[ 1 - \frac{r^2}{H_{\text{comp}}^2} \right], \quad (\text{B1})$$

$$g = \frac{4\pi}{3} G d_0 r \left[ 1 - \frac{3}{5} \frac{r^2}{H_{\text{comp}}^2} \right], \quad (\text{B2})$$

$$T_a(r, t) = T_L(c(t)) \left[ 1 + \gamma \frac{c(t)^2 - r^2}{H_{\text{comp}}^2} \right], \quad (\text{B3})$$

$$\mu_a = \mu_{\text{ICB}} - \frac{2\pi}{3} G d_0 \beta (r^2 - c^2) \equiv \mu_{\text{ICB}} + \mu', \quad (\text{B4})$$

with  $c(t)$  the time-dependent radius of the inner core and  $H_{\text{comp}}^2 = 3K_0/2\pi G d_0^2$  which is obtained (see Table 3) from fitting Eq. (B1) to PREM (Dziewonski and Anderson, 1981) after removal of the ICB density jump.  $K_0$  and  $d_0$  are the bulk modulus and density at the center, respectively.  $\gamma$  is the assumed constant Grüneisen parameter (Vočadlo et al., 2003). The expression for temperature can be obtained from a limited expansion of the expression in Labrosse et al. (2001). Eq. (B4) comes from Eq. (12) of Lister and Buffett (1995) using Eq. (B2) and keeping only the leading order.  $\beta$  is the coefficient of compositional expansion, assumed constant and computed from the compositional contribution  $\Delta_\xi d$  to the density jump across the ICB as (Braginsky and Roberts, 1995; Lister and Buffett, 1995)

$$\beta \equiv -\frac{1}{d} \left( \frac{\partial d}{\partial \xi} \right)_{P,S} = d \left( \frac{\partial \mu}{\partial P} \right)_{S,\xi} = \frac{\Delta_\xi d}{d_\xi}. \quad (\text{B5})$$

Note the sign difference in the definition of  $\beta$  between that of Lister and Buffett (1995) and that of Braginsky and Roberts (1995). For consistency with the coefficient of thermal expansion the latter choice is made here.

The thermal expansion coefficient  $\alpha$  is computed using

$$\alpha = \frac{\gamma d C_p}{K_S} \quad (\text{B6})$$

with  $C_p$  the heat capacity at constant pressure.  $K_S$  and therefore  $\alpha$  both vary with radial position (see Labrosse, 2003, for details) and can be written to second order as

$$K_S = K_0 \left( 1 - \frac{8r^2}{5H_{\text{comp}}^2} \right). \quad (\text{B7})$$

$$\alpha = \alpha_0 \left( 1 + \frac{3r^2}{5H_{\text{comp}}^2} \right). \quad (\text{B8})$$

The central values,  $\alpha_0$  and  $K_0$  are obtained from the density parameters using Eq. (B6) and the definition of  $H_{\text{comp}}$ , respectively. These two profiles only enter in the computation of the dissipation due to conduction along the isentrope.

For an entirely liquid core, the isentropic temperature profile is parameterized by the central value as

$$T_a = T_0(t) \exp \left( -\gamma \frac{r^2}{H_{\text{comp}}^2} \right) \quad (\text{B9})$$

Using Eq. (31) for  $r = 0$  allows the computation of  $dT_0/dt$  for a given CMB heat flow.

## References

- Akahama, Y., Kawamura, H., 2004. High-pressure Raman spectroscopy of diamond anvils to 250 GPa: method for pressure determination in the multimegabar pressure range. *J. Appl. Phys.* 96, 3748.
- Alboussière, T., Ricard, Y., 2013. Reflections on dissipation associated with thermal convection. *J. Fluid Mech.* 725, R1.
- Alfè, D., Gillan, M.J., Price, G.D., 2002a. Composition and temperature of the Earth's core constrained by combining ab initio calculations and seismic data. *Earth Planet. Sci. Lett.* 195, 91–98.
- Alfè, D., Price, G.D., Gillan, M.J., 2002b. Iron under Earth's core conditions: liquid-state thermodynamics and high-pressure melting curve from ab initio calculations. *Phys. Rev. B* 65, 165118.
- Anderson, O.L., 1998. The Grüneisen parameter for iron at outer core conditions and the resulting conductive heat and power in the core. *Phys. Earth. Planet. Int.* 109, 179–197.
- Andraut, D., Bolfan-Casanova, N., Nigro, G.L., Bouhifd, M.A., Garbarino, G., Mezouar, M., 2011. Solidus and liquidus profiles of chondritic mantle: implication for melting of the Earth across its history. *Earth Planet. Sci. Lett.* 304, 251–259.
- Anzellini, S., Dewaele, A., Mezouar, M., Loubeyre, P., Morard, G., 2013. Melting of iron at Earth's inner core boundary based on fast X-ray diffraction. *Science* 340, 464–466.
- Aubert, J., Amit, H., Hulot, G., 2007. Detecting thermal boundary control in surface flows from numerical dynamos. *Phys. Earth Planet. Int.* 160, 143–156.

- Balchan, A.S., Drickamer, H.G., 1961. High pressure electrical resistance cell, and calibration points above 100 kilobars. *Rev. Sci. Instrum.* 32, 308–313.
- Balog, P.S., Secco, R.A., 1999. High pressure and temperature behaviour of electrical resistivity of hcp metals Ti, Zr and Gd. *J. Phys.: Condens. Matter* 11, 1273.
- Baroni, S., de Gironcoli, S., Dal Corso, A., Giannozzi, P., 2001. Phonons and related crystal properties from density-functional perturbation theory. *Rev. Mod. Phys.* 73, 515–562.
- Bastea, M., Mitchell, A.C., Nellis, W.J., 2001. High pressure insulator-metal transition in molecular fluid oxygen. *Phys. Rev. Lett.* 86, 3108–3111.
- Bi, Y., Tan, H., Jing, F., 2002. Electrical conductivity of iron under shock compression up to 200 GPa. *J. Phys.: Condens. Matter* 14, 10849–10854.
- Bohnenkamp, U., Sandström, R., Grimvall, G., 2002. Electrical resistivity of steels and face-centered-cubic iron. *J. Appl. Phys.* 92, 4402–4406.
- Braginsky, S.I., 1964. Magnetohydrodynamics of the Earth's core. *Geomag. Aeron.* 4, 898–916.
- Braginsky, S.I., Roberts, P.H., 1995. Equations governing convection in Earth's core and the geodynamo. *Geophys. Astrophys. Fluid Dyn.* 79, 1–97.
- Bridgman, P.W., 1957. Effects of pressure on binary alloys. *Proc. Am. Acad. Arts Sci.* 84, 131–216.
- Brummell, N.H., Clune, T.L., Toomre, J., 2002. Penetration and overshooting in turbulent compressible convection. *Astrophys. J.* 570, 825–854.
- Buffett, B.A., Huppert, H.E., Lister, J.R., Woods, A.W., 1992. Analytical model for solidification of the Earth's core. *Nature* 356, 329–331.
- Buffett, B.A., Huppert, H.E., Lister, J.R., Woods, A.W., 1996. On the thermal evolution of the Earth's core. *J. Geophys. Res.* 101, 7989–8006.
- Christensen, U.R., 2006. A deep dynamo generating Mercury's magnetic field. *Nature* 444, 1056–1058.
- Cusack, N., Enderby, J.E., 1960. A note on the resistivity of liquid alkali and noble metals. *Proc. Phys. Soc.* 75, 395–401.
- Davies, C.J., Gubbins, D., 2011. A buoyancy profile for the Earth's core. *Geophys. J. Int.* 187, 549–563.
- de Koker, N., Steinle-Neumann, G., Vlček, V., 2012. Electrical resistivity and thermal conductivity of liquid Fe alloys at high P and T, and heat flux in Earth's core. *Proc. Natl. Acad. Sci. USA* 190, 4070–4073.
- de Koker, N., Stixrude, L., 2009. Self-consistent thermodynamic description of silicate liquids, with application to shock melting of MgO periclase and MgSiO<sub>3</sub> perovskite. *Geophys. J. Int.* 178, 162–179.
- Dewaele, A., Loubeyre, P., Ocellif, F., Mezouar, M., Dorogokupets, P.I., Torrent, M., 2006. Quasihydrostatic equation of state of iron above 2 Mbar. *Phys. Rev. Lett.* 97, 215504.
- Dziewonski, A.M., Anderson, D.L., 1981. Preliminary reference Earth model. *Phys. Earth Planet. Inter.* 25, 297–356.
- Faber, T.E., 1972. *Introduction to the Theory of Liquid Metals*. Cambridge at the University Press.
- Fearn, D.R., Loper, D.E., 1981. Compositional convection and stratification of Earth's core. *Nature* 289, 393–394.
- Fiquet, G., Auzende, A.L., Siebert, J., Corgne, A., Bureau, H., Ozawa, H., Garbarino, G., 2010. Melting of peridotite to 140 gigapascals. *Science* 329, 1516–1518.
- Garg, A.B., Vijayakumar, V., Godwal, B.K., 2004. Electrical resistance measurements in a diamond anvil cell to 40 GPa on ytterbium. *Rev. Sci. Instrum.* 75, 2475–2478.
- Gonze, X., Amadon, B., Anglade, P.-M., Beuken, J.-M., Bottin, F., Boulanger, P., Bruneau, F., Caliste, D., Caracas, R., Côté, M., Deutsch, T., Genovese, L., Ghosez, Ph., Giantomassi, M., Goedecker, S., Hamann, D.R., Hermet, P., Jollet, F., Jomard, C., Leroux, S., Mancini, M., Mazevet, S., Oliveira, M.J.T., Onida, G., Pouillon, Y., Rangel, T., Rignanese, G.-M., Sangalli, D., Shaltaf, R., Torrent, M., Verstraete, M.J., Zerah, G., Zwanziger, J.W., 2009. ABINIT: first-principles approach to material and nanosystem properties. *Comput. Phys. Commun.* 180, 2582–2615.
- Gonze, X., Beuken, J.-M., Caracas, R., Detraux, F., Fuchs, M., Rignanese, G.-M., Sindic, L., Verstraete, M., Zerah, G., Jollet, F., Torrent, M., Roy, A., Mikami, M., Ghosez, Ph., Raty, J.-Y., Allan, D.C., 2002. First-principles computation of material properties, the ABINIT software project. *Comput. Mater. Sci.* 25, 478–492.
- Gonze, X., Rignanese, G.M., Caracas, R., 2005. First-principles studies of the lattice dynamics of crystals, and related properties. *Z. Kristallogr.* 220, 458–472.
- Gubbins, D., 1977. Energetics of the Earth's core. *J. Geophys.* 43, 453–464.
- Gubbins, D., 2007. Geomagnetic constraints on stratification at the top of Earth's core. *Earth Planets Space* 59, 661–664.
- Gubbins, D., Alfè, D., Masters, G., Price, G.D., Gillan, M.J., 2003. Can the Earth's dynamo run on heat alone? *Geophys. J. Int.* 155, 609–622.
- Gubbins, D., Alfè, D., Masters, G., Price, G.D., Gillan, M.J., 2004. Gross thermodynamics of 2-component core convection. *Geophys. J. Int.* 157, 1407–1414.
- Gubbins, D., Masters, T.G., Jacobs, J.A., 1979. Thermal evolution of the Earth's core. *Geophys. J. R., Astron. Soc.* 59, 57–99.
- Gubbins, D., Thomson, C.J., Whaler, K.A., 1982. Stable regions in the Earth's liquid core. *Geophys. J. R., Astron. Soc.* 68, 241–251.
- Gunnarsson, O., Calandra, M., Han, J.E., 2003. Colloquium: saturation of electrical resistivity. *Rev. Mod. Phys.* 75, 1085–1099.
- Gurvitch, M., 1981. Ioffe–Regel criterion and resistivity of metals. *Phys. Rev. B* 24, 7404–7407.
- Hurlburt, N.E., Toomre, J., Massaguer, J.M., Zahn, J.P., 1994. Penetration below a convective zone. *Astrophys. J.* 421, 245–260.
- Ioffe, A.F., Regel, A.R., 1960. Non-crystalline, amorphous and liquid electronic semiconductors. *Prog. Semicond.* 4, 237.
- Jaccard, D., Holmes, A.T., Behr, G., Inada, Y., Onuki, Y., 2002. Superconductivity of  $\epsilon$ -Fe: complete resistive transition. *Phys. Lett. A* 299, 282–286.
- Jarlborg, T., 2002. Ferromagnetic and antiferromagnetic spin fluctuations and superconductivity in the hcp-phase of Fe. *Phys. Lett. A* 300, 518–523.
- Keeler, R.N., Mitchell, A.C., 1969. Electrical conductivity, demagnetization, and the high-pressure phase transition in shock-compressed iron. *Solid State Commun.* 7, 271.
- Kohn, W., Sham, L.J., 1965. Self-consistent equations including exchange and correlation effects. *Phys. Rev.* 140, 1133A–1138A.
- Kono, M., Roberts, P., 2001. Definition of the Rayleigh number for geodynamo simulation. *Phys. Earth Planet. Inter.* 128, 13–24.
- Labrosse, S., 2003. Thermal and magnetic evolution of the Earth's core. *Phys. Earth Planet. Inter.* 140, 127–143.
- Labrosse, S., Hernlund, J.W., Coltice, N., 2007. A crystallizing dense magma ocean at the base of the Earth's mantle. *Nature* 450, 866–869.
- Labrosse, S., Poirier, J.-P., Le Mouél, J.-L., 1997. On cooling of the Earth's core. *Phys. Earth Planet. Inter.* 99, 1–17.
- Labrosse, S., Poirier, J.-P., Le Mouél, J.-L., 2001. The age of the inner core. *Earth Planet. Sci. Lett.* 190, 111–123.
- Lay, T., Hernlund, J., Buffett, B.A., 2008. Core–mantle boundary heat flow. *Nat. Geosci.* 1, 25–32.
- Linde, J.O., 1932. Elektrische Eigenschaften verdünnter Mischkristalllegierungen III. Widerstand von Kupfer- und Goldlegierungen. Gesetzmäßigkeiten der Widerstandserhöhungen. *Ann. Physik* 15, 219–248.
- Lister, J.R., 2003. Expressions for the dissipation driven by convection in the Earth's core. *Phys. Earth Planet. Inter.* 140, 145–158.
- Lister, J.R., 2004. Thermal winds forced by inhomogeneous boundary conditions in rotating, stratified, hydromagnetic fluid. *J. Fluid Mech.* 505, 163–178.
- Lister, J.R., Buffett, B.A., 1995. The strength and efficiency of the thermal and compositional convection in the geodynamo. *Phys. Earth Planet. Inter.* 91, 17–30.
- Lister, J.R., Buffett, B.A., 1998. Stratification of the outer core at the core–mantle boundary. *Phys. Earth Planet. Inter.* 105, 5–19.
- Loper, D.E., 1978a. The gravitationally powered dynamo. *Geophys. J. R., Astron. Soc.* 54, 389–404.
- Loper, D.E., 1978b. Some thermal consequences of a gravitationally powered dynamo. *J. Geophys. Res.* 83, 5961–5970.
- McDonough, W.F., 2003. Compositional model for the Earth's core. In: Carlson, R.W. (Ed.), *Treatise on Geochemistry*. Elsevier–Pergamon, Oxford, pp. 547–568.
- Matassov, G., 1977. *The electrical conductivity of iron-silicon alloys at high pressures and the Earth's core*, Thesis. Lawrence Livermore Lab., Univ. California.
- Mertig, I., 1999. Transport properties of dilute alloys. *Rep. Prog. Phys.* 62, 237–276.
- Milchberg, H.M., Freeman, R.R., Davey, S.C., 1988. Resistivity of simple metal from room temperature to 10<sup>6</sup> K. *Phys. Rev. Lett.* 61, 2364–2367.
- Monkhorst, H.J., Pack, J.D., 1976. Special points for Brillouin-zone integrations. *Phys. Rev. B* 13, 5188–5192.
- Mooij, J.H., 1973. Electrical conduction in concentrated disordered transition metal alloys. *Phys. Status Solidi A* 17, 521–530.
- Mosenfelder, J.L., Asimow, P.D., Ahrens, T.J., 2007. Thermodynamic properties of Mg<sub>2</sub>SiO<sub>4</sub> liquid at ultra-high pressures from shock measurements to 200 GPa on forsterite and wadsleyite. *J. Geophys. Res.* 112, B06208.
- Mott, N.F., 1936. The electrical resistance of dilute solid solutions. *Proc. Cambridge Philos. Soc.* 32, 281.
- Mott, N.F., 1972. The electrical resistivity of liquid transition metals. *Philos. Mag.* 26, 1249.
- Murthy, V.R., Westrenen, W.V., Fei, Y., 2003. Experimental evidence that potassium is a substantial radioactive heat source in planetary cores. *Nature* 423, 163–165.
- Nasu, S., Sasaki, T., Kawakami, T., Tsutsui, T., Endo, S., 2002. Mössbauer study of  $\epsilon$ -Fe under an external magnetic field. *J. Phys.: Condens. Matter* 14, 11167–11171.
- Nimmo, F., 2007. *Treatise on Geophysics, Core dynamics*, Elsevier, vol. 8, pp. 253–303 (chap. 2–Energetics of the core).
- Nimmo, F., Price, G.D., Brodholt, J., Gubbins, D., 2004. The influence of potassium on core and geodynamo evolution. *Geophys. J. Int.* 156, 363–376.
- Nishi, T., Shibata, H., Waseda, Y., Ohta, H., 2003. Thermal conductivities of molten iron, cobalt, and nickel by laser flash method. *Metall. Mater. Trans. A* 34, 2801–2807.
- Nomura, R., Ozawa, H., Tateno, S., Hirose, K., Hernlund, J., Muto, S., Ishii, H., Hiraoka, N., 2011. Spin crossover and iron-rich silicate melt in the Earth's deep mantle. *Nature* 473, 199–202.
- Norbury, A.L., 1921. The electrical resistivity of dilute metallic solid solutions. *Trans. Faraday Soc.* 16, 570–596.
- Ohno, H., 1971. Antiferromagnetism in hcp iron-ruthenium and hcp iron-osmium alloys. *J. Phys. Soc. Jpn.* 31, 92–101.
- Perdew, J.P., Burke, K., Ernzerhof, M., 1996. Generalized gradient approximation made simple. *Phys. Rev. Lett.* 77, 3865–3868.
- Poirier, J.P., 2000. *Introduction to the Physics of the Earth's Interior*, 2nd ed. Cambridge University Press.
- Poirier, J.P., Shankland, T.J., 1993. Dislocation melting of iron and temperature of the inner core boundary, revisited. *Geophys. J. Int.* 115, 147–151.
- Pozzo, M., Davies, C., Gubbins, D., Alfè, D., 2012. Thermal and electrical conductivity of iron at earth's core conditions. *Nature* 485, 355–358.
- Pozzo, M., Davies, C., Gubbins, D., Alfè, D., 2013. Transport properties for liquid silicon-oxygen-iron mixtures at Earth's core conditions. *Phys. Rev. B* 87, 014110.
- Reichlin, R.L., 1983. Measuring the electrical resistance of metals to 40 GPa in the diamond-anvil cell. *Rev. Sci. Instrum.* 54, 1674–1677.

- Rogers, T.M., Glatzmaier, G.A., Jones, C.A., 2006. Numerical simulations of penetration and overshoot in the sun. *Astrophys. J.* 653, 765–773.
- Sata, N., Hirose, K., Shen, G., Nakajima, Y., Ohishi, Y., Hirao, N., 2010. Compression of FeSi, Fe<sub>3</sub>C, Fe<sub>0.95</sub>O, and FeS under the core pressures and implication for light element in the Earth's core. *J. Geophys. Res.* 115, B09204.
- Savrasov, S.Y., Savrasov, D.Y., 1996. Electron-phonon interactions and related physical properties of metals from linear-response theory. *Phys. Rev. B* 54, 16487–16501.
- Secco, R.A., Schloessin, H.H., 1989. The electrical resistivity of solid and liquid Fe at pressure up to 7 GPa. *J. Geophys. Res.* 94, 5887–5894.
- Sha, X., Cohen, R.E., 2011. First-principles studies of electrical resistivity of iron under pressure. *J. Phys.: Condens. Matter* 23, 075401.
- Stacey, F.D., 1993. Thermodynamics relationships and the properties of iron at earth's core conditions, in: *Conference proceedings for the Association for the International Advancement of High Pressure Colorado Springs, Colorado*.
- Stacey, F.D., Anderson, O.L., 2001. Electrical and thermal conductivities of Fe–Ni–Si alloy under core conditions. *Phys. Earth Planet. Inter.* 124, 153–162.
- Stacey, F.D., Davis, P.M., 2008. *Physics of the Earth*, 4th ed. Cambridge University Press.
- Stacey, F.D., Loper, D.E., 2007. A revised estimate of the conductivity of iron alloy at high pressure and implications for the core energy balance. *Phys. Earth Planet. Inter.* 161, 13–18.
- Stanley, S., Bloxham, J., Hutchinson, W.E., Zuber, M.T., 2005. Thin shell dynamo models consistent with Mercury's weak observed magnetic field. *Earth Planet. Sci. Lett.* 234, 27–38.
- Stanley, S., Mohammadi, A., 2008. Effects of an outer thin stably stratified layer on planetary dynamos. *Phys. Earth Planet. Inter.* 168, 179–190.
- Stevenson, D.J., 1983. Planetary magnetic fields. *Rep. Prog. Phys.* 46, 555–620.
- Stevenson, D.J., 2003. Planetary magnetic fields. *Earth Planet. Sci. Lett.* 208, 1–11.
- Stixrude, L., de Koker, N., Sun, N., Mookherjee, M., 2009. Thermodynamics of silicate liquids in the deep Earth. *Earth Planet. Sci. Lett.* 278, 226–232.
- Turner, J.S., 1973. *Buoyancy Effects in Fluids*. Cambridge, p. 368.
- Van Zytveld, J.B., 1980. Electrical resistivities of liquid transition metals. *J. Phys. Colloq. Orsay Fr.* 41, C8.503–C8.506.
- Vočadlo, L., Alfè, D., Gillan, M.J., Price, G.D., 2003. The properties of iron under core conditions from first principles calculations. *Phys. Earth Planet. Inter.* 140, 101–125.
- Wiesmann, H., Gurvitch, M., Lutz, H., Ghosh, A., Schwarz, B., Strongin, M., Allen, P.B., Halley, J.W., 1977. Simple model for characterizing the electrical resistivity in A-15 superconductors. *Phys. Rev. Lett.* 38, 782–785.
- Zahn, J.P., 1991. Convective penetration in stellar interiors. *Astron. Astrophys.* 252, 179–188.